Faculty
of Science

Palacký University
Olomouc

PALACKÝ UNIVERSITY OLOMOUC

FACULTY OF SCIENCE

DEPARTMENT OF PHYSICAL CHEMISTRY

Structure and electronic properties at the α-Fe_2O_3/Pt interface

Master's Thesis

Author : Bc. Adam Matěj

Supervisor : Piotr Błoński, Ph.D.

Academic year : 2018/2019

Olomouc 2019

Declaration

I hereby declare that I elaborated this thesis myself and that all data presented here are true. I also declare that I used all sources cited herein.

Olomouc :..... .....

Handwritten signature

Acknowledgement

Chciałbym podziękować mojemu promotorowi, Panu Doktorowi Piotrowi Błońskiemu, za nieocenioną pomoc, wartościowe rady oraz ogromną cierpliwość. Praca pod jego przewodnictwem była dla mnie wspaniałą lekcją, którą wykorzystam w moim przyszłych badaniach i publikacjach. Jeszcze raz bardzo dziękuję.

Velké díky patří panu profesorovi Michalu Otyepkovi za možnost pracovat na tomto velmi zajímavém tématu. Dále za možnost vyjet na studijní pobyt, kde jsem mohl studovat a pracovat pod vedením Davida Beljonna.

J'aimerais remercier Dr David Beljonne, Dr Jérôme Cornil et Dr David Cornil des discussions et de leurs précieux conseils.

Rád bych také poděkoval doktoru Štěpánovi Kmentovi za vřelou komunikaci ohledně experimentálních výsledků.

J'aimerais dédier ce mémoire à ma merveilleuse copine, qui me soutenait de tout son cœur dans les moments difficiles.

Dále bych chtěl svou práci věnovat svojí rodině, která mne bezmezně podporovala během celého studia a vždy mi byla oporou.

Last, but not least, I would like to thank to all my friends, who supported and helped me throughout my studies and my stay in Belgium. Namely : Janča a Rosťa, kteří se mnou diskutovali technické problémy (děkuji!), všichni kamarádi z magisterského studia, the whole group of ESN Mons (merci & motashakr awi), Federica and Enrica (grazie), Kaylan (thank you), Isaac (merci). Special thanks to Bára (děkuji) and Zuzia (dziękuję bardzo) for translations.

I would like to acknowledge this project as a part of the IGA_PrF_2019_031 grant.

Bibliographic Identification

Author :	Bc. Adam Matěj
Title :	Structure and electronic properties at the α-Fe_2O_3/Pt interface
Thesis :	Master's
Supervisor :	Piotr Błoński, Ph.D.
Year of defense :	2019
Department :	Physical Chemistry
Abstract :	This work focuses on (0001) α-Fe_2O_3 (hematite) in combination with (111) platinum as a possible material for photoelectrochemical (PEC) water splitting. We used DFT+U calculations to provide insight into the electronic properties in such heterostructure. We constructed two different interfaces and a Pt-doped slab to study the effect of interface and doping on electronic properties. Both heterostructures were found to be stable and exhibited an interface-induced continuum of states through bandgap increasing conductivity between the two layers. Heterostructure with O-terminated interface exhibited superior electronic properties such as increased charge separation and migration of charge carriers towards desired sides of the structure. Doping with Pt led to states around Fermi level and caused higher electron-hole recombination rate. This theoretical study helps to understand changes and processes happening at the Fe_2O_3/Pt interface leading to improved materials for PEC water splitting.
Keywords :	hematite, platinum, heterostructure, DFT, photoelectrochemistry, interface
Pages :	52
Language :	English

Bibliografická identifikace

Autor :	Bc. Adam Matěj
Název :	Struktura a elektronické vlastnosti rozhraní α-Fe_2O_3/Pt
Typ práce :	Diplomová
Vedoucí :	Piotr Błoński, Ph.D.
Rok obhajoby :	2019
Pracoviště :	Katedra fyzikální chemie

Abstrakt : Tato práce je zaměřena na rozhraní (0001) α-Fe_2O_3 (hematit) v kombinaci s (111) platinou jako možným materiálem pro fotoelektrochemický (PEC) rozklad vody. K popisu elektronické struktury těchto heterostruktur jsme použili DFT+U výpočty. Vytvořili jsme dvě různá rozhraní a platinou dopovaný povrch, abychom mohli zkoumat efekty rozhraní a dopace na elektronické vlastnosti. Obě heterostruktury jsou stabilní a vykazují rozhraním indukované kontinuum stavů, které zvyšuje vodivost mezi oběma vrstvami. Kyslíkem terminovaná heterostruktura vykazuje vyjímečné vlastnosti, zejména zvýšenou separaci nábojů a jejich migraci k požadovaným stranám materiálu. Dopace atomem platiny vede ke vzniku stavů okoli Fermiho hladiny a způsobuje vyšší rekombinaci elektronů a děr. Tato teoretická práce pomáhá porozumět změnám a procesům, ke kterým dochází na rozhraní Fe_2O_3/Pt, a které vedou k vylepšení materiálů pro použití k fotoelektrochemickému štěpení vody.

Klíčová slova :	hematit, platina, heterostruktura, DFT, fotoelektrochemie, rozhraní
Počet stran :	52
Jazyk :	Angličtina

Table of Contents

1. Introduction 7

2. Theoretical Part 11

2.1. Quantum Mechanics 11

2.2. Density Functional Theory 13

2.2.1. Kohn-Sham Equations 15

2.2.2. Exchange-Correlation Functionals 16

2.3. Computational Chemistry 19

2.3.1. Basis sets 19

2.3.2. Pseudopotentials and PAW 20

2.3.3. Reciprocal Lattice 21

3. Computational Details 24

3.1. Methodology 24

3.2. Convergence 25

3.3. Structures 27

4. Results and Discussion 29

4.1. Bulk Structures 29

4.2. Slabs 31

4.3. Heterostructures 36

4.4. Pt-doped Hematite 43

5. Summary 45

6. Závěr 47

7. Bibliography 49

1. Introduction

It is now a widely accepted fact that human activity causes global warming. Humankind in its current phase grows rapidly, using modern technologies invented in the last few decades. Not so long time ago, the total number of people reached seven billion, and it is not going to stop there. An increasing population means a growing demand for energy as one of the main pillars of modern society and this problem concerns numerous scientific groups around the globe. New, renewable and effective energy providing methods are necessary to sustain the growth since the burning of fossil fuels is one of the causes of global warming.

Several renewable energy sources are known nowadays. Yet, mastering the energy harvesting methods is not a simple task. Truly promising, although challenging is the conversion of solar energy. The Sun provides our planet with an enormous amount of energy. Nature figured out a way to collect it and convert it into chemical energy in the form of chemical bonds. Now, the man tries to copy the work of nature once again for his own use. Scientists are currently on a good starting point in this pursuit of "free" energy. They know perfectly the theory behind the processes of photosynthesis and with all the modern tools, they also succeeded in the creation of various devices [1, 2]. This achievement opened different ways of solar energy conversion. However, they all have common requirements. In order for them to be widely applied, the devices must be cost-effective, efficient and nature-friendly. A promising solution is a photoelectrochemical (PEC) water splitting method [3–6], which uses the energy of photons to break water molecules into hydrogen and oxygen gases. These can then be used to generate electricity in hydrogen-fuel cells. A scheme of a PEC cell is illustrated in figure 1.

The crucial part of PEC cells is the construction of the photo-electrodes, where photoinduced electron-hole pairs are created. Photo-electrodes are semiconductors with a desirable width of bandgap, together with the required position of the gap compared to the normal hydrogen electrode (NHE). The bandgap must be greater than the potential of O_2/H_2O, which is 1.23 V against the NHE at pH=0. The optimal position of the bandgap is so that the standard potentials of both half reactions lie within the gap. Otherwise, bias voltage must be applied in order to shift the positions of valence and conductive bands. If the material fulfils these

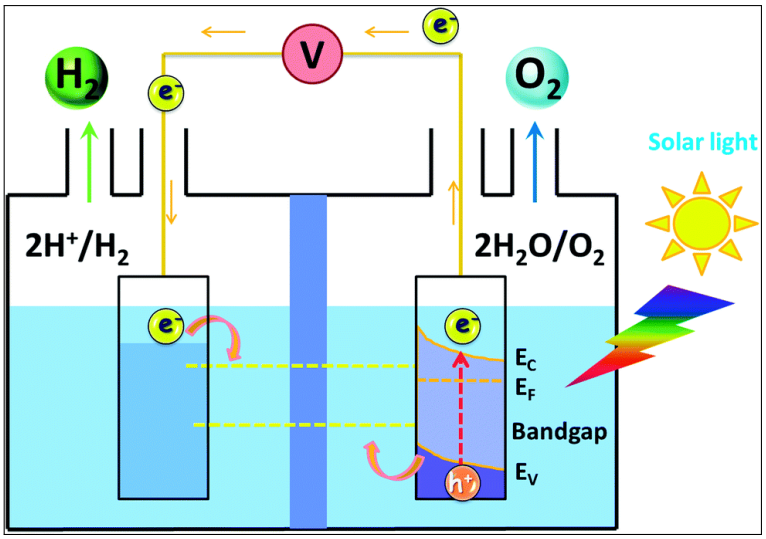

Figure 1 – *Scheme showing the processes during PEC water splitting. The yellow horizontal dashed lines illustrate redox potentials for O_2/H_2O (lower) and $2H^+/H_2$ (upper), respectively. E_C and E_V denote conductive and valence band, respectively. E_F is the Fermi level. Here the photo-active electrode is an anode, where the holes migrate onto the surface and oxidize water molecules into oxygen molecules. This reaction is called oxygen evolution reaction (OER). Reprinted from ref. [5]*

requirements, it should also be a good absorber, meaning that it absorbs a wide part of the spectrum for higher photon-to-electron conversion yield. Other important factors describing the material's suitability are surface catalytic properties, electron-hole recombination rate, electric conductivity, stability and price. While the perfect material satisfying all abovementioned requirements for the best performance stays undiscovered, various known materials can be modified and combined resulting in higher efficiency.

One material, in particular, receives high attention of the scientific community for its obvious benefits. It is the most stable iron oxide - α-hematite. It is naturally abundant, non-toxic and offers suitable bandgap of 2.2 eV [3]. Despite its numerous drawbacks (bandgap position, low hole diffusion length, high electron-hole recombination, low oxidation kinetics), it seems to be a possible candidate with high potential for photoanode material. It is due to the fact that most of the drawbacks can be suppressed in some way. Probably the most serious problems are low hole diffusion length (∼5-10 nm), high electron-hole recombination rate and low conductivity. These effects are linked together and can be explained by the presence of surface trap states [7–9]. The hole diffusion towards the surface is a key factor for a

successful OER. Its low value limits the effective thickness of the hematite layer to few nanometers but even the optimal thickness does not ensure effective migration of holes into the electrolyte. The surface trap states are the reason for that. Several ways of overcoming this sluggish migration were proposed [10, 11], including passivation, doping or adding a layer of co-catalyst. On the other side of the hematite layer, electrons are required to migrate towards the conductive back contact, which leads them towards cathode for H^+ reduction. Here the connection between hematite and the conductive scaffolding is crucial in order to maximize the electron transport. Therefore, any trap states at the interface are undesirable while a conductive interface helps to increase the electron migration.

This work studies the influence of platinum layer as a potential substrate for hematite, reducing electron-hole recombination rate. The aim of this research is to provide theoretical support for experiments on this photoanode material and to describe the observed behaviour on an atomistic level. It was found out by an ongoing experiment [12], that hematite shows superior properties when grown on a platinum substrate in comparison with other, more complex substrates, e.g. widely used fluorine-doped tin oxide FTO. In order to provide deeper insights into the questions from the experiment, we conducted a thorough analysis of the interface, looking into structural changes and electronic properties arising from the heterojunction. We employed density functional theory (DFT) simulations to describe the electronic structure and structural properties of interest. Spin-polarized calculations with projector augmented wave (PAW) formalism were carried out using the Vienna Ab-initio Simulation Package (VASP). This work is divided into four parts. Firstly, the bulk structure of hematite and platinum were modelled in order to get a base for further calculations. The calculations parameters were tested in a convergence study on these bulk materials. Electronic properties under investigation were the density of states (DOS), bandstructure and Bader charge analysis. Magnetic properties of hematite were also included. Secondly, thin layers (slabs) were modelled to represent the surfaces of both materials. Workfunction was calculated herein to broaden the analysis and local DOS (LDOS) are presented to better understand the electronic changes with the creation of the surface. LDOS here was layer and orbital-resolved to maximally illustrate the electronic structure. Geometry changes were evaluated

using the mean absolute percentage error (MAPE). In the third part, the hematite and platinum layers formed a heterostructure. The detailed study of properties of the interface is presented and discussed here using the same evaluation procedure as for slabs. The data obtained were compared with both slab and bulk results. In the fourth part, a Pt-doped hematite surface was studied as a possible surface modification towards better PEC performance.

2. Theoretical Part

2.1. Quantum Mechanics

During the late 19^{th} century, there seemed to be little left to be discovered in physics. Newton's equations of motion together with Maxwell's electrodynamics seemed satisfactory for the description of the world's problems. Nonetheless, a great commotion was on the doorstep with experiments on the radiation of the black body and photo-electric effect. Max Planck came first with the idea of quantized energy. Although his findings supported the measurements of the radiation of the black body, this theory was too revolutionary and it has not been given enough recognition. It was later when Albert Einstein studied the photoelectric effect. He used Planck's findings of quantized energy to explain the experiment and realized, that not only it gave the explanation, but he also obtained the same value of Planck's constant. This was the first sign that there was still a lot to be discovered in physics. Einstein described light as particles and found out that this particle has zero rest mass. With his findings and Planck's formula, he formulated equation 1 :

$$E = h\nu, \tag{1}$$

which says that the quantum of energy is proportional to the frequency of the wave and Planck constant. Louis de Broglie expressed the wavelength through Einstein equation for relativistic energy and Einstein-Planck equation (eq. 1), yielding the de Broglie wavelength :

$$E = mc^2 = h\nu = \frac{hc}{\lambda} \qquad \lambda = \frac{h}{mc} = \frac{h}{p}. \tag{2}$$

Through this relation, de Broglie postulated that every particle with momentum has also its wavelength. This was the beginning of the theory that we nowadays know as the wave-particle duality. The idea of energy having only discrete values did not commute with classical mechanics and therefore there needed to be a way to connect them. The foundation of quantum mechanics was laid by Erwin Schrödinger who formulated the time-dependent Schrödinger equation (eq. 3) which describes the

evolution of a system in time.

$$i\hbar\frac{d}{dt}\Psi(t) = \widehat{H}\Psi(t). \tag{3}$$

In order to describe stationary states of the system, we can derive the time-independent Schrödinger equation which has the following form :

$$\widehat{H}\Psi = E\Psi. \tag{4}$$

In eq. 4 $\widehat{H}$ is the Hamiltonian operator acting on the wavefunction Ψ. The wavefunction is also sometimes called the state and it is the eigenfunction of $\widehat{H}$. Its eigenvalue is then the energy of the particular state. Each state can result in several energies from which the lowest one describes the ground state of the system. If we solve eq. 4 numerically, we obtain the ground state. For that, we need to know the form of $\widehat{H}$. Since the observable quantity represented by Hamiltonian is energy, it consists of kinetic $\widehat{T}$ and potential $\widehat{V}$ energy operators (eq. 5).

$$\widehat{H} = \widehat{T} + \widehat{V} \tag{5}$$

Both operators for kinetic and potential energy act on all particles i in the system as shown in eq. 6-7

$$\widehat{T_i} = \frac{-\hbar}{2m_i}\Delta_i = \frac{-\hbar}{2m_i}\left(\frac{\partial^2}{\partial x_i^2} + \frac{\partial^2}{\partial y_i^2} + \frac{\partial^2}{\partial z_i^2}\right) \tag{6}$$

$$\widehat{V} = \widehat{V}_{NN} + \widehat{V}_{Ne} + \widehat{V}_{ee} = \frac{1}{4\pi\epsilon_0}\left(\sum_i\sum_{i'>i}\frac{Z_i Z_{i'} e^2}{|R_i - R_{i'}|} + \sum_i\sum_j\frac{Z_i e^2}{|R_i - r_j|} + \sum_j\sum_{j'>j}\frac{e^2}{|r_j - r_{j'}|}\right) \tag{7}$$

Lower indexes NN, Ne and ee denote potential energy between two nuclei, nucleus and electron and between two electrons, respectively. Schrödinger equation can be solved analytically only for the hydrogen atom where we consider the interaction between a proton and an electron. We can separate independent variables and interpret the molecular Hamiltonian as the sum of two separate Hamiltonians for nuclei and electrons. The separation of these two Hamiltonians is justified by the Born-Oppenheimer approximation (BOA) which simplifies the solution without significant

error. The electronic Hamiltonian can be solved independently because the mass of a nucleus is much higher than that of an electron, thus electrons move much faster than nuclei and the nuclear motion is taken as independent of the electronic motion. Then we solve the electronic wavefunction for every nuclear geometry and the total wavefunction is given by the product of the electronic and nuclear wavefunctions. For any system with more than one electron, the wavefunction cannot be solved analytically and we must accept further approximations. The total electronic wavefunction can be approximately described as a product of one-electron wavefunctions. This approximation gives rise to an error originating in the neglection of electron-electron interaction. This is due to the fact that all the electrons in the system are correlated and their dynamics are dependent on each other. There are several methods for calculating wavefunctions using the variational principle and solving correlation energy afterwards. These methods are called *ab-initio* because, in the beginning, they need only physical constants like mass fo electron, Planck's constant etc. They can be really precise but the computational cost is so high that they can be used only for small systems. Further problem is that some of these methods are not size consistent, which means that for larger systems one needs even more demanding calculations. The limitation of methods based on wavefunction solutions is precision versus applicability in the meaning of the size of the system. Nonetheless, there is another method of how to calculate the total energy of the system without solving the electronic wavefunction. This method is using electron density instead and thus is called density functional theory. This method is described in the next chapter.

2.2. Density Functional Theory

Density functional theory, or DFT in short, is a widely used go-to method for the electronic structure of larger systems [13, 14]. It is a function of 3 coordinates for density $\rho(r)$ while wavefunction methods are functions of 3N coordinates.

$$\rho(r) = N \int |\Psi(r_1, r_2, ..., r_N)|^2 dr_2 ... dr_N \tag{8}$$

$\rho(r)$ represents the probability of finding any electron in dr. It is a natural number and the probability is normalized such as :

$$\int \rho dr = N. \tag{9}$$

Calculating electron density instead of the electronic wavefunction allows us to solve the electronic structure on a larger scale with higher chemical interest. The precision is based on the functional used which will be discussed later in this chapter.

The foundation of DFT was published in 1964 by Hohenberg and Kohn [15] who presented two theorems giving DFT physical robustness. First one states : "*The external potential* $V_{ext}(r)$ *is (to within a constant) a unique functional of* $\rho(r)$ *; since, in turn* $V_{ext}(r)$ *fixes* $\widehat{H}$ *we see that the full many particle ground state is a unique functional of* $\rho(r)$." Here the $V_{ext}(r)$ is in term of Hamiltonian the interaction of electrons with Coulombic potential of nuclei. This is the only contribution to the Hamiltonian which does not come solely from electrons ($\widehat{V}_{NN}$ equals to a constant in BOA) and thus it determines the Hamiltonian. Another important consequence from this theorem is that the true electronic ground state is a functional of the electron density $\rho(r)$ so we can write :

$$E_0[\rho_0] = T[\rho_0] + V_{ee}[\rho_0] + V_{ext}[\rho_0]. \tag{10}$$

The external potential can be simplified into a one-electron term because the external potential is the same for each electron. The first two terms are functionals of electrons and they can be written together as Hohenberg-Kohn functional. We can then rewrite eq. 10 as follows :

$$E_0[\rho_0] = F_{HK}[\rho_0] + \int \rho_0(r) V_{Ne} dr. \tag{11}$$

Here the problem is the F_{HK} because we do not know its correct form.

Even if we did know its correct form we still miss the correct electron density. The second Hohenberg-Kohn theorem helps on finding the electron density : "*For a given* V_{ext} *there is a given electron density* ρ_0*. Then for any other electron density*

ρ' *the energy will be higher.*" This can be written as

$$E[\rho_0] < E[\rho']. \tag{12}$$

This is nothing else than a variational principle which allows us to change the electron density until we find the ground state. Here we have the manual on how to find the correct electron density, but the correct functional is still a mystery. The first idea of how to construct the functional came one year later in a work by Kohn and Sham.

2.2.1. Kohn-Sham Equations

Kohn and Sham [16] presented one-electron wavefunctions for non-interacting system :

$$F_{KS}\varphi_i = \varepsilon_i\varphi_i, \tag{13}$$

where F_{KS} is a Kohn-Sham functional :

$$F_{KS} = -\frac{1}{2}\Delta_i + V_s(r). \tag{14}$$

Here $V_s(r)$ is the potential of the non-interacting system. In order to find the potential we write the energy functional for our real system :

$$E[\rho(r)] = T_n[\rho] + J[\rho] + F_{XC}[\rho] + \int V_{Ne}\rho(r)dr. \tag{15}$$

$T_n[\rho]$ is kinetic energy of non-interacting system, $J[\rho]$ is coulombic interaction, $V_{Ne}\rho(r)dr$ is the external potential and $F_{XC}[\rho]$ is the exchange-correlation functional which contains everything we do not know :

$$F_{XC}[\rho] = T[\rho] - T_n[\rho] + V_{ee}[\rho] - J[\rho]. \tag{16}$$

The form of the exchange-correlation functional is unknown, and its approximations will be discussed in the next chapter. If we now apply the variational principle to eq. 15 to find the energies of one-electron wavefunctions [17] (orbitals), we see that

they are the same as Kohn-Sham equations. We now find the form of $V_s(r)$ as

$$V_s(r) = \int \frac{\rho(r_2)}{r_{12}} dr_2 - \sum_A^M \frac{Z_A}{r_{1A}} + V_{XC}(r_1). \tag{17}$$

Once we know all terms in eq. 17, we can insert the $V_s(r)$ into the one-electron wavefunctions, that give us the ground state orbitals, thus the ground state electron density which we can then insert into eq. 15 and get the ground-state energy. The only problem is still the V_{XC}, which is simply defined as

$$V_{XC} = \frac{\delta E_{XC}}{\delta \rho}, \tag{18}$$

which says that the exchange-correlation potential is a functional derivative of exchange-correlation functional and thus has to be solved iteratively with respect to energy. This procedure is based on the variational principle (eq. 12), and the method is called the self-consistent field (SCF). Because we are unable to solve the Hamiltonian directly, we take the road of guess and adjust. The general scheme of the SCF method is shown in figure 2. Based on the input geometry, an initial guess for wavefunction is used for density calculation. This guess density is then used to solve the Hamiltonian and to produce a new density, which reacts to the potential of the previous density. Then the comparison between the initial and current density is done based on our criterion. If the change is small enough, the SCF loop ends. Otherwise, it goes back to solve the Hamiltonian.

2.2.2. Exchange-Correlation Functionals

As stated above, we do not know the form of the F_{XC}. Hence we try to substitute it with other known parameters which we can calculate. There is a vast amount of various functionals, and some can reach high accuracy and agreement with experiments. Yet, there is none that can be used universally with desired precision. The problem with universal correctness is simple. Developers of these functionals form them in such a way, so they work well for their systems. A good functional for metals does not have to work well for organic compounds etc. This is also caused by the fact that the functional includes a part of error compensation arising from approximations in the potential and kinetic energy terms, and these errors are not

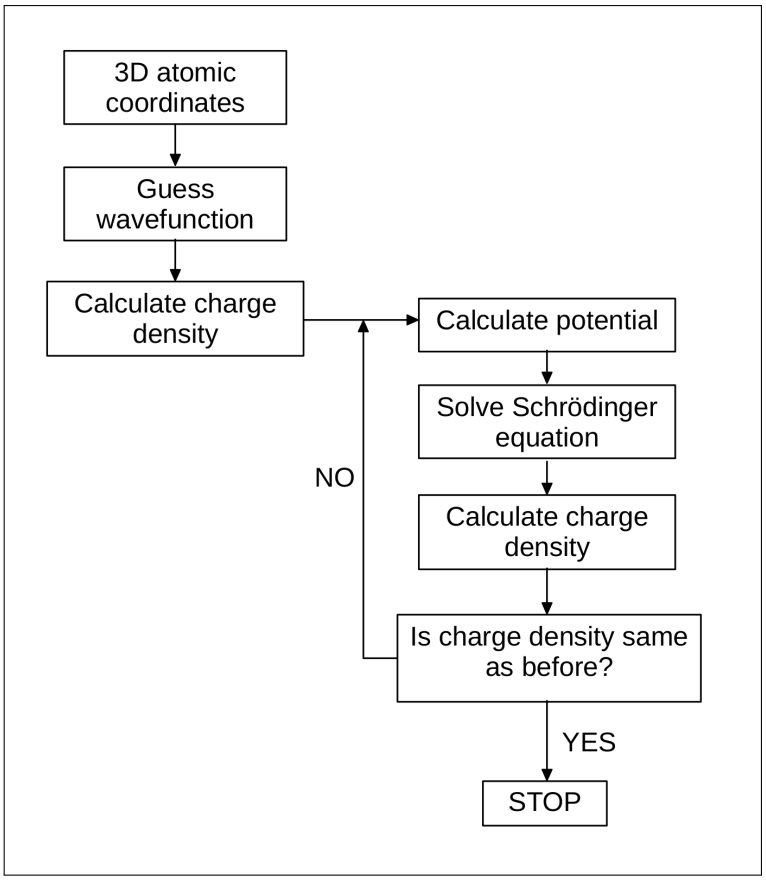

Figure 2 – *The algorithm for the SCF method.*

consistent throughout different systems.

The exchange-correlation functional can be expressed in the form of expansion into a series of density gradients. Leaving a zero-order term in the expansion leads to the approximation of local density known as the LDA. Including terms of higher orders generates further approximations, by definition more precise than the LDA. They are namely : generalized gradient approximation (GGA), meta-GGA and hybrid functionals, which is a specific case discussed below. LDA deals only with the electron density at the point of interrest [18]. It is applicable for systems with homogeneous density, i.e. solid state physics, but gives a high error for systems of chemical interest. The improvement towards more universal usage (systems with non-homogeneous density), is made by the GGA, i.e. GGA includes a dependence of the exchange-correlation functional on the local gradient of the electron density [19].

Functionals using GGA give better results in molecular systems and ground-state calculations, than those based on LDA. Functionals from the GGA family are widely used for their balance between accuracy and affordable computational needs, which

allows the study of large systems including hundreds of atoms. Next approximation following GGA, is the meta-GGA, which depends on the Laplacian and the derivation of the kinetic energy of the electron density [20]. A further approximation is a hybrid functional method [21], which includes part of HF energy together with DFT. These functionals can give results of a great agreement with experiments however, they are not universal. It is because the ratio between HF and DFT is mixed just so it matches the property of interest. Then, the certain ratio of HF and DFT for a precise description of bandgap may fail for optimization of bond lengths or other parameters. The reason behind including HF is that HF method gives the exact exchange energy. The correlation functional is built in such a way, that it cancels part of the error arising from the approximate exchange functional (in DFT). Then, if the exchange functional is described purely by HF exchange, the total error would not be necessarily smaller than with pure DFT, thus only a part of HF is used in the exchange functional. The ratio between HF and DFT differs, e.g. 25 % HF and 75 % PBE is used in HSE06 functional. Hybrids have higher computational demands but give usually better results than GGA.

DFT can be widely used to study the electronic structure with great success but fails to describe accurately the bandstructure of Mott insulators. Hendrik de Boer and Verwey noticed in 1937 [22], that some transition metal oxides, predicted to be conductors, are, in fact, insulators. After this, Mott suggested, that this is due to the electron-electron interactions [23,24], which are not covered in the tight-binding model. The Hamiltonian contains only a transfer integral in the kinetic term, which describes hopping of electrons between atoms during conduction but it does not include electron-electron interactions. Electrons are located at their atoms and strong Coulomb repulsion hinders hopping. These materials are strongly correlated, and their properties have to be described with other methods. One of the simplest ways of correcting this failure of DFT was presented in the 1960s by John Hubbard [25]. Hubbard model contains a potential term with on-site interactions in the Hamiltonian, which improves the strong correlation of electrons in Mott insulators.

2.3. Computational Chemistry

As mentioned above, the wavefunction and/or electron density of the ground state unambiguously describes observable properties of the system. The physical foundation was presented in previous chapters while important parameters and further approximations with their applications are described herein. With the development of computers and quantum mechanics, it became possible to study materials on a sub-atomic level. Computational chemistry is based on a physical description of the system, which results in observable chemical properties.

2.3.1. Basis sets

In order to simplify the operations on wavefunction, we represent the wavefunction by a set of known functions. These functions are then called basis sets and differ with the area of use. For chemistry, the basis functions are usually atomic orbitals (AOs), which then produce molecular orbitals (MO) through linear combination. This method is well known to chemists as the MO-LCAO method. Atomic orbitals can be represented using various functions, for example Gaussians, centered at the atomic nuclei. Several variations of basis sets [26, 27] using AO were developed to increase the accuracy and to sufficiently describe the behaviour of the system (e.g. polarizability [28]). Another way of substituting the electronic wavefunction is a set of plane-waves. The plane-wave representation has several advantages against AOs, especially in solid-state physics. It is due to the fact that calculations on 3-dimensional periodic systems, such as crystals, can be performed much more efficiently using plane-waves [29]. The main reason to that is the Bloch's theorem [30] which says that in a periodic potencial of nuclei (periodic crystal lattice) the electron potential is also periodic. Then the electronic wavefunction is identical to the Bloch wave which is simply said a plane-wave multiplied by a periodic function (wavevector). This periodic function represents the periodicity of the crystal and thus extends the plane wave through the lattice. The accuracy of the AOs is based on the number of functions that describe each AO. In the plane-waves basis sets, their number and so the accuracy of the calculation is governed by the energy cut-off. It has to be specified in the calculation and the basis set includes all the plane-waves with their energy up to the cut-off. The electronic wavefunction is then a Fourier transfor of

the plane-waves. The expansion of the electronic wave functions in plane waves is computationally very efficient : fast Fourier transofrm (FFT) allows a change from a real-space (the potential energy is diagonal), to momentum-space (the kinetic energy is diagonal).

2.3.2. Pseudopotentials and PAW

As shown earlier, the total electron wavefunction is a product of one-electron wavefunctions solved for each electron in the system. This means that for heavier atoms more wavefunctions have to be solved. In order to truncate the number of electrons, we can focus only on valence electrons, which are of the highest interest, and replace the core electrons with a representative potential. This approximation is called frozen core and is also often called as pseudopotential (PP) approximation [31]. The idea behind frozen core potential comes from the complexity of the oscilating wavefucntion of core electrons. Inner electrons are much closer to the nucleus than valence electrons and thus exhibit stronger interaction. The wavefunctions then oscilate rapidly (fig. 3 - blue Ψ) because of the requirement of their orthogonality. Pseudopotentials are calculated on isolated atoms and the inner region, limited by distance r_c, is represented by smooth function. The outer region is identical to valence electrons potential and the two functions are matched in value and derivation at the r_c point. This approximation effectively lowers the computational costs, but lowers the accuracy and brings numerous parameters into the calculation.

An accurate method for description of all-electron system is linearized augmented plane-wave (LAPW). The unit cell is divided into non-overlapping atom-centered spheres and interstitial space between these spheres. Inside the spheres, atomic-like functions describe the all-electron system. The interstitial space is described by LAPWs which connect the functions inside each sphere. In comparison with PP the LAPW method reaches higher accuracy by including all electrons in the calculation which in turn results into more demanding calculations.

In 1994, Blöchl generalized both abovementioned methods into one [33]. His work presented the projector-augmented wave (PAW) method which allows the use of frozen core pseudopotentials with higher accuracy. It is achieved through transformation of pseudo wavefunction into all electron wavefunction with projector function.

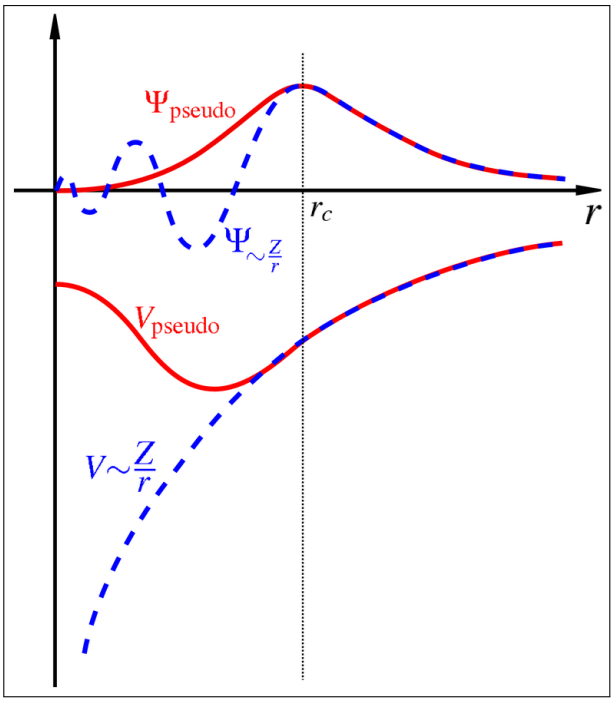

Figure 3 – *Illustration of the difference between pseudopotential, V_{pseudo}, and real potential (blue), as well as pseudo wavefunction and real wavefucntion, red and blue Ψ. Reprinted from ref. [32]*

This transformation happens only inside the cut-off radius, similarly to PP core region. Outside of the core region the wavefunctions of PP and LAPW are identical. The result of this transformation is effectivity of PP and accuracy of LAPW. Smoother wavefunction requires lower cut-off energy for the basis set i.e. the highest frequency in Fourier transform. For effective calculations of solid state problems [34], Kresse and Joubert [35] presented a way to implement plane-waves into the PAW method.

2.3.3. Reciprocal Lattice

In the case of periodic structures, i.e. crystals, it is usefull to perform the calculations in the reciprocal space where it is easier to implement Bloch's theorem and symmetry [36]. A reciprocal space is a Fourier transform of a real space and is also called a k-space. The reciprocal space is especially usefull for diffraction and band theory, which is explained by Laue and Brillouin. First we need to define the reciprocal lattice with respect to the real (direct) lattice. In crystalography, any lattice can be described as a Bravais lattice, giving the minimal image of the crystal, which

can be periodically transformed into an infinite crystal. It is defined by :

$$R = u_1 a_1 + u_2 a_2 + u_3 a_3, \tag{19}$$

where R is a position vector, u_i are integers and a_i are primitive vectors of given lattice. Similarly the reciprocal position vector is written as

$$G = v_1 b_1 + v_2 b_2 + v_3 b_3 \tag{20}$$

where v_i are integers, and b_i are reciprocal lattice vectors. The relation between primitive and reciprocal vectors is

$$b_i \cdot a_j = 2\pi\delta_{ij} \tag{21}$$

and $\delta_{ij} = 1$ if $i = j$ and $\delta_{ij} = 0$ if $i \neq j$. Laue showed the geometrical representation of diffraction theory by Laue's equations :

$$\begin{gathered} a_1 \cdot \Delta k = 2\pi v_1 \qquad a_2 \cdot \Delta k = 2\pi v_2 \qquad a_3 \cdot \Delta k = 2\pi v_3 \\ for \quad \Delta k = G \end{gathered} \tag{22}$$

where Δk is scattering vector. It gives the diffraction conditions based on the lattice vectors. Brillouin further stated the diffraction conditions in the description of electron band theory. The first step is construction of Brillouin zone. It is defined as a Wigner-Seitz primitive cell in the reciprocal lattice. The first Brillouin zone is the smallest volume entirely enclosed by planes that are the perpendicular bisectors of the reciprocal lattice vectors drawn from the origin. Then any wave whose wave-vector drawn from the origin terminates on the surface of the Brillouin zone will be diffracted. These characteristics of the reciprocal space explain why is it usefull to calculate for example electron band-structure in reciprocal rather than in real space. Bloch's theorem together with Brillouin zone support the concept of the electron band structure. The band structure is a consequence of Pauli exclusion principle which says that two electrons cannot occupy an orbital with the same energy. And in crystals, there are $N \sim 10^{23}$ electrons that must occupy orbitals of different energies. Then, the accessible energies are not a discrete lines like in atoms but rather

a continuum of states. Then electrons with similar energy, or we can say similar wavevector occupy same band. The band-structure allows us to see if the material is a metal, an insulator or rather a semiconductor with direct or indirect bandgap. In order to be able to visualize the band-structure we need to specify the path along k-points of interest with enough steps between them. K-points are high symmetry points (or critical points) in the first Brillouin zone and we can visualize only the values of energy along the line from one point to another. A typical band-structure of silicon is shown in figure 4.

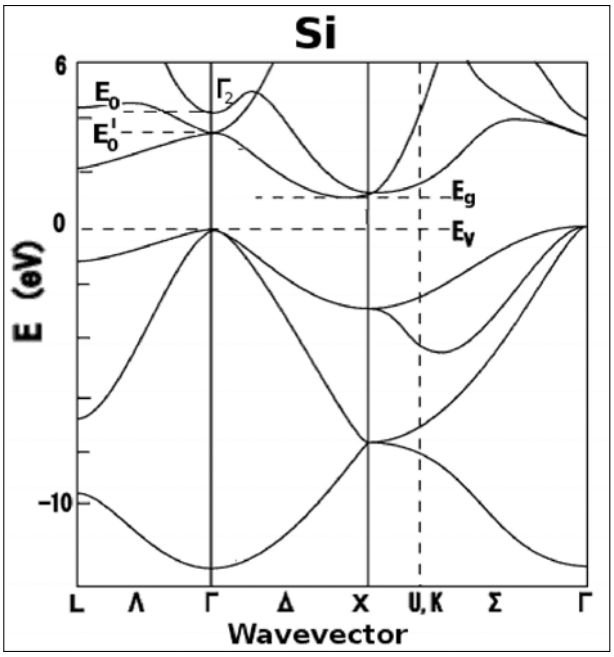

Figure 4 – *Band-structure of Si showing indirect bandgap between* Γ *and* X *k-points. Reprinted from thesis by Nicolas Large [37]*

3. Computational Details

3.1. Methodology

All simulations were carried out using PBE functional [19] in VASP program with periodic boundary conditions. Due to the magnetic properties of iron oxide, the calculations were spin-polarized. VASP is mostly aimed at solid-state physics of periodic structures and therefore it works with a plane-wave basis set. Pseudopotentials with PAW formalism were used. For a better description of the electronic structure, the iron atoms were described by 14 electrons ($3p^6$ $3d^7$ $4s^1$) with the semi-core $3p$ orbitals being treated as valence. Oxygen and platinum atoms were described by pseudopotentials with 6 and 10 valence electrons, respectively.

Hematite's strongly correlated d electrons were described using the Hubbard model. The form of Hubbard Hamiltonian is then,

$$H = -t \sum_{<j,l>\sigma} c^{\dagger}_{j\sigma} c_{l\sigma} + U \sum_{j} n_{j\uparrow} n_{j\downarrow} - \mu \sum_{j} (n_{j\uparrow} + n_{j\downarrow}). \tag{23}$$

The first term is the kinetic energy, the second term is the interaction energy between the electrons on the same occupied site and the last term is the chemical potential controlling the filling. In VASP, two main approaches are implemented for the Hubbard method. The first one is Liechtenstein's [38] with the form shown below

$$E_{dc}(\hat{n}) = \frac{U}{2} \hat{n}_{tot}(\hat{n}_{tot} - 1) - \frac{J}{2} \sum_{\sigma} \hat{n}^{\sigma}_{tot}(\hat{n}^{\sigma}_{tot} - 1). \tag{24}$$

This formalism requires setting for two parameters : U - effective on-site Coulomb interaction and J - effective on-site exchange interaction. A second approach was presented by Dudarev et al. [39] and the formalism is shown in equation 24.

$$E_{GGA+U} = E_{GGA} + \frac{(U-J)}{2} \sum_{\sigma} \left[\left(\sum_{m1} n^{\sigma}_{m1,m2} \right) - \left(\sum_{m1,m2} n^{\sigma}_{m1,m2} n^{\sigma}_{m2,m1} \right) \right] .) \tag{25}$$

Here it is clear that U and J do not enter separately and $U - J$ can be used as U_{eff}. Throughout this paper, U is be used instead of U_{eff} since J was set to 0 eV. The choice of U value depends on the properties that one wants to study. In this

work, the effect of U was checked against DOS, magnetic moments and structural parameters. The value of U was chosen to reproduce reasonable results for DOS and magnetic moments and the same value was used throughout all calculations for bulk and slab structures. The U value was set to 4.3 eV and on-site corrections were applied only to Fe atoms.

3.2. Convergence

To obtain precise and reliable results, a convergence study is necessary for each system. Convergence tests according to cut-off, k-points sampling and U value were done herein. Cut-off energy and k-points are mutually independent, therefore they were tested independently with the other value lower to speed up the calculations. Once these parameters have been set, U was tested on chosen values from previous convergence tests. The convergence study was performed on bulk hematite with the structure specified in the following part.

Cut-off energy convergence test (fig. 5) was done for values 350 - 600 eV in steps of 25 eV. K-points mesh was generated in format $x \times x \times x$ in range 4-20. Evaluation

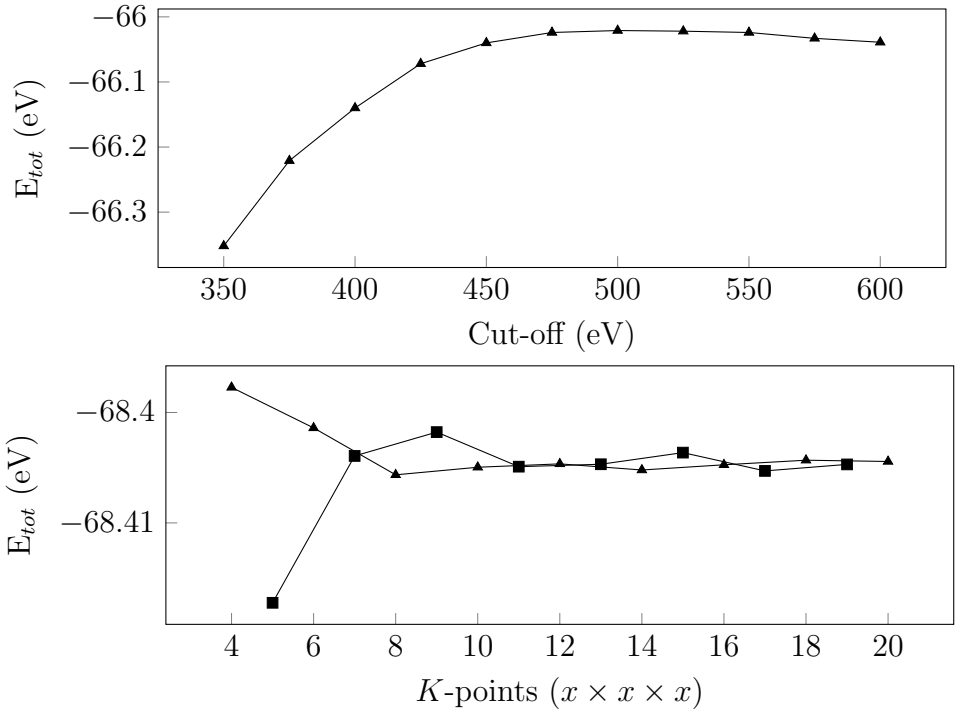

Figure 5 – *Energy plotted as a function of cut-off energy and K-points, respectively. In the case of k-points, odd and even divisions are plotted separately to show bigger energy changes in odd divisions.*

of the results led to working values for cut-off energy of 525 eV, for which the change of E_{tot} was less than 0.01 kcal/mol. K-points mesh was set to $12 \times 12 \times 12$ for energy calculations, where the change in energy was again less than 0.01 kcal/mol. For DOS calculations, a $16 \times 16 \times 16$ mesh was chosen, more dense grids did not show changes in DOS plots. Energy values from odd numbers deviate more than these from even numbers. For this reason, further calculations were carried out using even numbers.

Both cut-off and k-points were calculated using fixed U at 4 eV as a good initial approximation according to literature [40–45]. After setting the first two parameters, the convergence of on-site correction was done in range 2-8 eV in steps of 0.5 eV and 0.1 eV between 4 and 5. Figure 6 shows the change in bandgap and magnetic moments with increasing U. A U value of 4.3 eV provided good agreement with

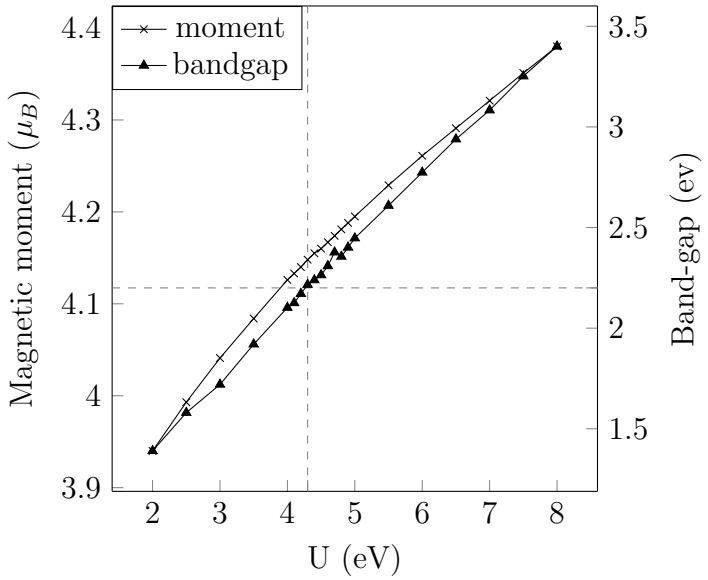

Figure 6 – *Bandgaps and magnetic moments as functions of U. Calculated at constant structure parameter. Dashed lines are shown to guide the eye. The vertical line shows value 4.3 eV for U, used for further calculations. The horizontal line shows experimental bandgap with value of 2.2 eV.*

literature, including experimental bandgap values [3, 46] and magnetic moments [47,48], therefore this value was chosen for further calculations. As mentioned before, the on-site correction parameter also affects the structure and its effect is shown in figure 7. Volume versus U dependance differed from literature [49] in equilibrium volumes but kept the same curve shape. This might be caused by using different methods (functionals, pseudopotentials, minimization method).

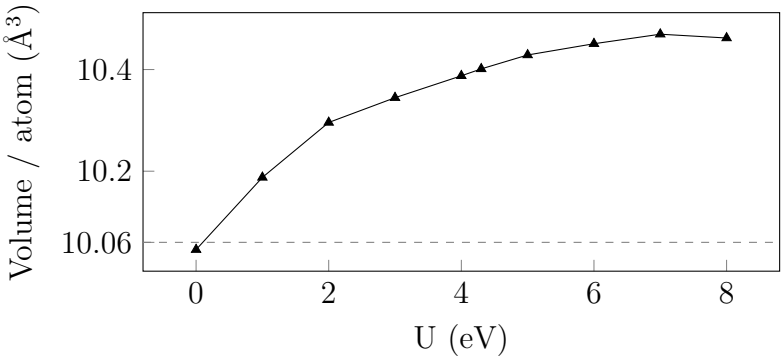

Figure 7 – *Volume as a function of U parameter. The dashed horizontal line shows experimentally found cell volume. U=0 eV corresponds to PBE without on-site correction.*

3.3. Structures

Hematite bulk structure was optimized using rhombohedral primitive cell with experimental lattice vectors [50] : $a = 5.035$ Å, $c = 5.427$ Å. The volume of the cell was gradually increased, ions relaxed in their positions and the total energy was calculated. Then, using the Birch-Murnaghan equation of state [51], the optimal volume per atom was found to be 10.40 Å^3. Electronic properties were calculated on the hexagonal unit cell with lattice parameters : $a = 5.081$ Å, $c = 13.871$ Å. Bulk platinum was modelled using experimental lattice vector for face-centered cubic (FCC) unit cell [52] : $a = 3.923$ Å, which, after optimization, was found to be $a = 3.969$ Å. Within the optimized cells, ions were allowed to relax their positions. Unit cells of bulk structures contained 10/30 atoms for hematite rhombohedral and hexagonal cells, respectively, and 4 atoms for platinum. In the case of thin layers, bulk structures were cleaved in [0001] and [111] directions for hematite and platinum to form desired surfaces of the slabs. The (0001) hematite and (111) platinum surfaces were created following work by Neufeld et al. [45] where they found the optimal lattice vectors in order to minimise the lattice mismatch between hematite and platinum. The lattice vectors used are then : $a = 4.980$ Å, $b = 8.630$ Å and c was set to 32 Å as a satisfying layer of vacuum. The misfit is 2.25 % on Pt and 2.3 % for hematite lattices. In the case of hematite, non-stoichiometric slabs of 6 Fe-layers with two different terminations were prepared. These two slabs contained 54 and 66 atoms in Fe and O-terminated slabs, respectively. The platinum layer was represented by a slab of four atomic layers with (111) surface containing 24

atoms. Slab structures are illustrated in figure 8. All slabs structures were relaxed in

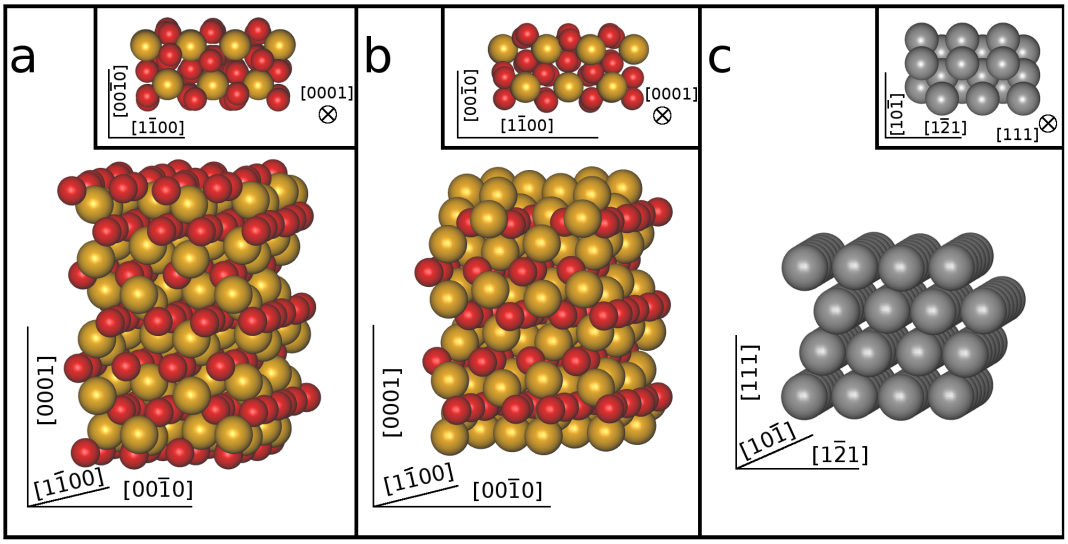

Figure 8 – *a) An O-terminated oxide layer, inset shows the view from the top ; b) Fe-terminated layer created by deleting two frontier oxygen layers ; c) Pt slab with a thickness of four atomic layers. Illustrated structures are after geometry optimization. Red, gold and grey balls represent oxygen, iron and platinum atoms, respectively. Miller indexes are shown for better orientation in the direction of the cells.*

order to correctly describe free surfaces and their electronic structure. The resulting heterostructures were created by joining the platinum slab with hematite slabs of both terminations. The heterostructures were gradually optimized in order to find the optimal interface geometry.

4. Results and Discussion

4.1. Bulk Structures

The optimization of the bulk unit cell volumes of both Fe_2O_3 and Pt showed an increase compared to the experimentally found values by 3.2 and 1.2 %, respectively. The volume was increased by changing the lattice vectors while the ratio between them was held constant. The variation of energy with respect to cell volume for different antiferromagnetic (AFM) ordering is shown in fig. 9 a. The α-hematite is

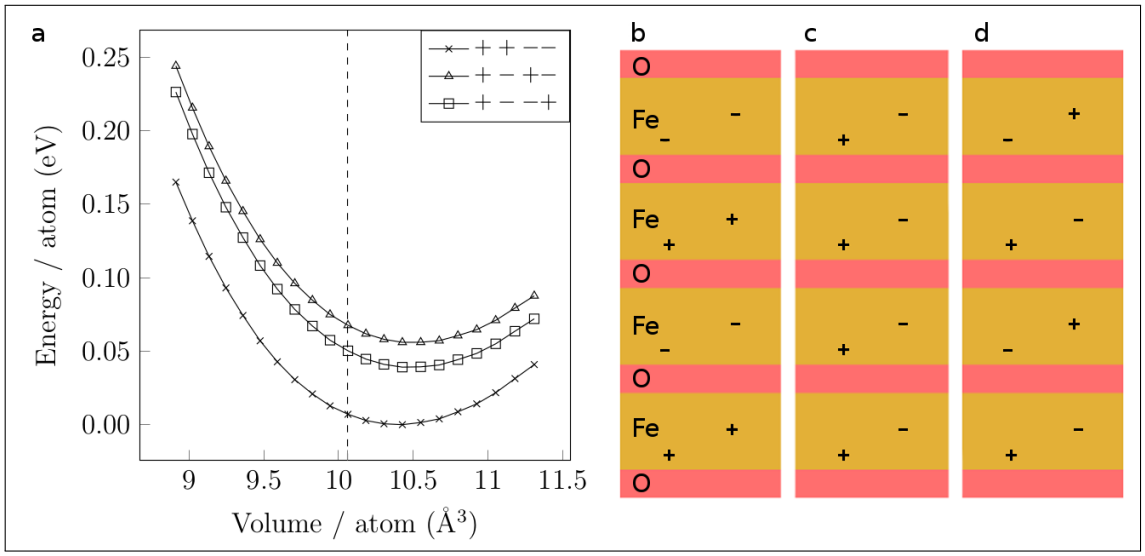

Figure 9 – *(a) shows the dependency of total energy on cell volume for three different AFM orderings. The dashed line marks experimental volume at 10.06 Å. The energy is relative to the lowest value which is taken as zero. Possible forms of AFM structure are illustrated (b)-(d) where the order corresponds to the graph.*

antiferromagnetic below the Morin temperature; for α-hematite it is 250 K. Morin temperature is characteristic for hematite and tells at which temperature the magnetic phase transition from antiferromagnetism to weak ferromagnetism occurs. There are multiple ways of organizing the magnetic moments in the AFM unit cell. The options are illustrated in figure 9 b-d. The minimum energy corresponds to "long-range" AFM ordering (fig. 9 b), where the orientation of the magnetic moments is alike within an iron layer and alternates through the crystal. Iron atoms in bulk α-Fe_2O_3 show a magnetic moment of 4.15 μ_B, which is close to the experimental values of 4.6-4.9 μ_B [47, 48]. The geometry of the relaxed bulk oxide was taken as a foundation for comparison of geometrical changes in slabs and heterostructures.

The measured values are namely : O-O and Fe-Fe distances, Fe-O bond-length, O..O layer distance and O-Fe-O bond angle. The results are summarized in table 1. The

Table 1 – *Summary of chosen structural values of bulk hematite. Distances are given in Angströms.*

Structure	Fe-O	Fe-Fe	O-O	O..O	∡O-Fe-O
Bulk	1.962	2.996	2.693	2.312	102.53 °

optimized lattice parameter of FCC bulk platinum differs only by 1.2 % from the experimental value (fig. 10) and shows no changes in electronic structure.

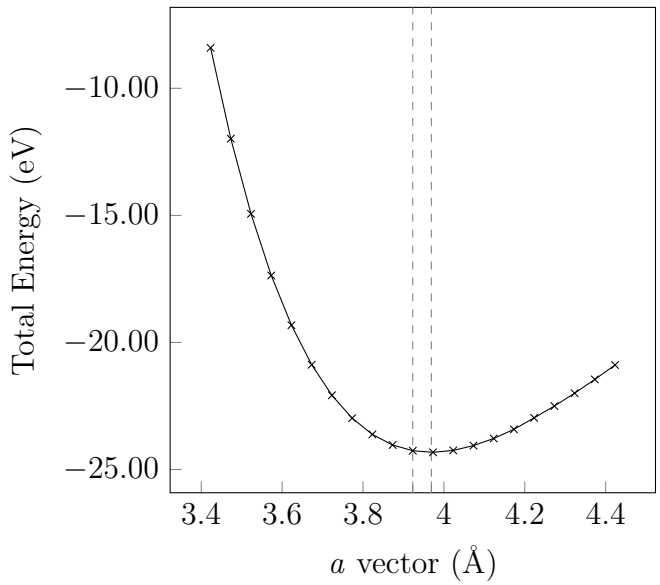

Figure 10 – *The dependence of E_{tot} on lattice parameter for FCC bulk platinum. The vertical dashed lines show experimental volume and optimal cell dimension, respectively.*

The electronic structure of bulk hematite was analysed through the density of states and bandstructure plots as well as Bader charge analysis [53–55]. Total DOS plot and bandstructure (fig. 11) for bulk α-Fe_2O_3 show indirect bandgap of 2.2 eV. Bader charge analysis was conducted in order to study the charge distribution between atoms. Results show that each oxygen atom receives 0.30 e per Fe-O bond, summing in the total charge of -1.20 e per oxygen. Each iron atom bonds with six oxygens, and each oxygen with four irons. Therefore, the total charge on each iron atom is +1.80 e. In bulk hematite, the total charge of each Fe and O layer, in this unit cell, is ±7.20 e.

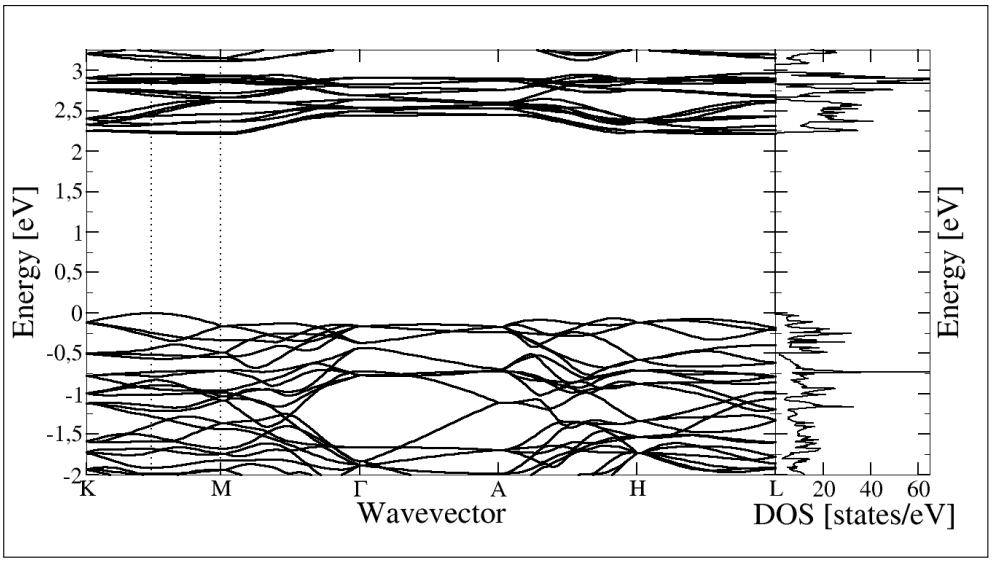

Figure 11 – *Bandstructure and total DOS of bulk α-Fe_2O_3 with a bandgap of 2.2 eV. Fermi energy is set to zero. Positions of indirect bandgap are marked by vertical dashed lines; conductive band minimum (M point), valence band maximum (between K and M points.*

4.2. Slabs

In order to simulate thin layers, slab structures were prepared as described above. Hematite layer was cleaved to expose (0001) surface having a thickness of six Fe layers. Two different, non-stoichiometric and non-polar terminations of oxide surface were prepared and their properties compared. The first one was O-rich termination, sometimes named in the literature as -FeO_3. This surface was reported as the most stable [56]. The second surface was Fe-terminated which was created by deleting the frontier O layers from the previously described structure. These slabs are referred to as O-O and Fe-Fe throughout this work, describing the terminations on both sides of the slab. Platinum was cleaved in the [111] direction containing four atomic layers. Both unit cells were created with the same lattice vectors. All surfaces were allowed to relax by gradually tightening the optimization criteria until the forces acting on atoms were less than 1 meV/atom.

The platinum surface shows minimal geometry changes while considerable surface reconstruction happens on both oxide surfaces. Measured values are shown in table 2 together with their mean absolute percentage errors (MAPE). Structural changes at the surface for both oxide slabs vary from 0.6 to 12.6 % where the highest changes are observed for positions of Fe atoms closest to the surface. Two values with especially

Table 2 – *Atom distances, bond lengths and angles at the surface layer of both slabs showing the surface reconstruction. Distances are given in Angströms. Values in brackets are MAPE in % always compared with bulk values.*

Structure	Fe-O	Fe-Fe	O-O	O..O	∡O-Fe-O
Bulk	1.962	2.996	2.693	2.312	102.53 °
O-O	1.754 (11.86 %)	2.887 (3.78 %)	2.676 (0.64 %)	2.185 (5.81 %)	99.44 ° (3.11 %)
Fe-Fe	1.883 (4.20 %)	3.083 (2.82 %)	2.606 (3.34 %)	2.446 (5.48 %)	117.32 ° (12.61 %)

high MAPE compared to bulk values are Fe-O bond length in O-terminated slab (11.86 %) and O-Fe-O bond angle (12.61 %) in Fe-terminated slab. The first is caused by shortening the oxygen layers distance by almost 6 %, which results in more densely packed monolayer. Latter mentioned a change of almost 15° is caused by the iron atoms being much closer to the oxygen layer in order to stabilize the free surface. It is clear from the results that both surfaces are stabilized by a contraction in a direction perpendicular to the surface.

The electronic structures of both slabs exhibit the appearance of states within the bandgap. In the case of O-O slab, new states around the Fermi level lower the bandgap to only 0.37 eV. DOS for O-O slab is shown in figure 12 a. Total DOS shows the electronic structure of the whole slab and red and blue curves only two frontier layers of one side of the slab. If two layers of the opposite side of the slab were plotted, the spins would flip. The difference of spin originates in the AFM ordering in the oxide slab. It can be seen that the midgap states disappear gradually with the distance from the surface. All states between -0.2 to ∼1.75 eV originate from the free surface and after further investigation, it was found that they are both present on O and Fe atoms with higher contribution from iron (fig. 12 b). Presence on both elements shows strong hybridization between all surface atoms. These surface states would effectively lower the PEC activity with the photo-induced electrons having low energy altogether with the localization of these excited electrons onto the surface. Truly narrow midgap states, around 0.25 eV, with sharp edges demonstrate strong localization. Close positioning from both sides of the Fermi level implies that these states can act as both electron and hole traps. Trapping of both charge carriers onto the surface would lead to higher recombination rate, which is highly undesirable. The bandstructure (fig. 13) shows that the bandgap of 0.37 eV is direct at the Γ point. One can notice from figures 12-13 the difference of the electronic structure

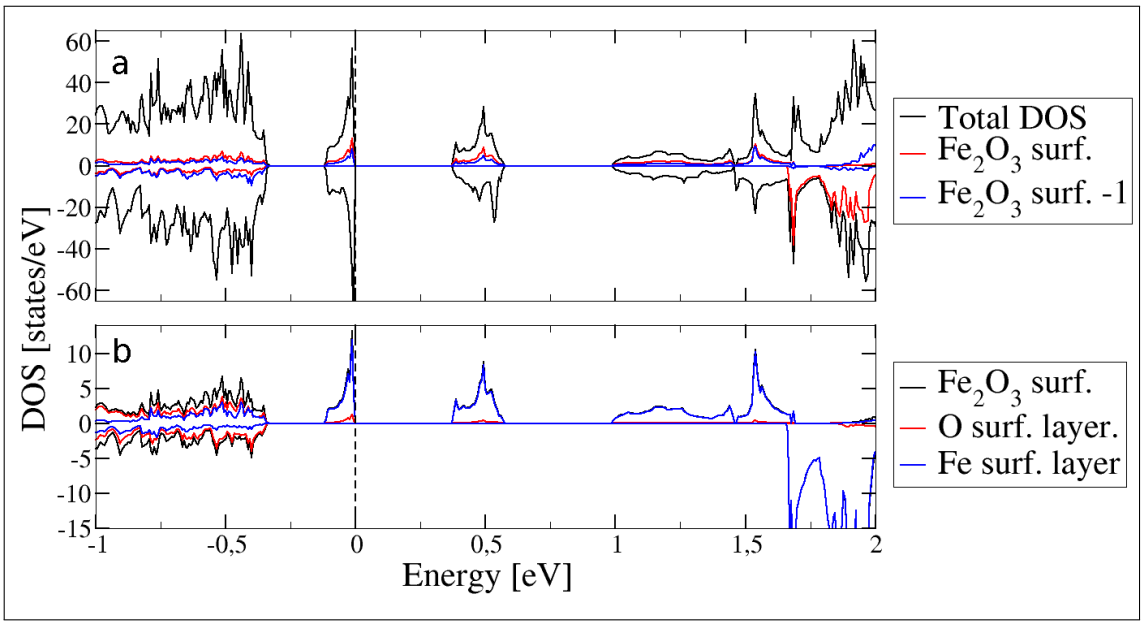

Figure 12 – *(a) total DOS (black) and LDOS for O-O slab. LDOS for frontier Fe_2O_3 monolayer (red) and for second outer-most monolayer (blue). (b) LDOS contributions from O (red) and Fe (blue) in the first Fe_2O_3 monolayer. Fermi energy is set to zero, marked by the vertical dashed line.*

for a different spin. While one can see mid-gap states in spin up, a wide bandgap (1.67 eV) is present in spin down. The mid-gap states decrease towards bulk, already almost disappearing in the third layer. The spin is opposite on the other surface of the same slab, and it is due to the presence of opposite magnetic moment at the Fe layer closest to the surface. This phenomenon is studied and used in the field of spintronics, where it is required to have different bandgap or conductivity for each spin. Although the use of hematite for spintronics is a question of time [57], the outcomes of the surface creation mean a drawback in the PEC application. The surface as created here shows bandgap too small, below the energy needed for water splitting.

The electronic structure of Fe-terminated slab exhibits some similarities with its more stable counterpart, especially in the really narrow bandgap in spin up while preserving wider bandgap in spin down, as shown in figure 14 (red and blue). The spin up bandgap is lowered to 0.22 eV while spin down bandgap is 1.8 eV wide with a low number of states in the conductive band in the surface layer. This results in a higher concentration of excited electrons in the bulk layers. The surface states in spin down are localized mostly on Fe atoms in the first layer (fig. 14 b), which resembles

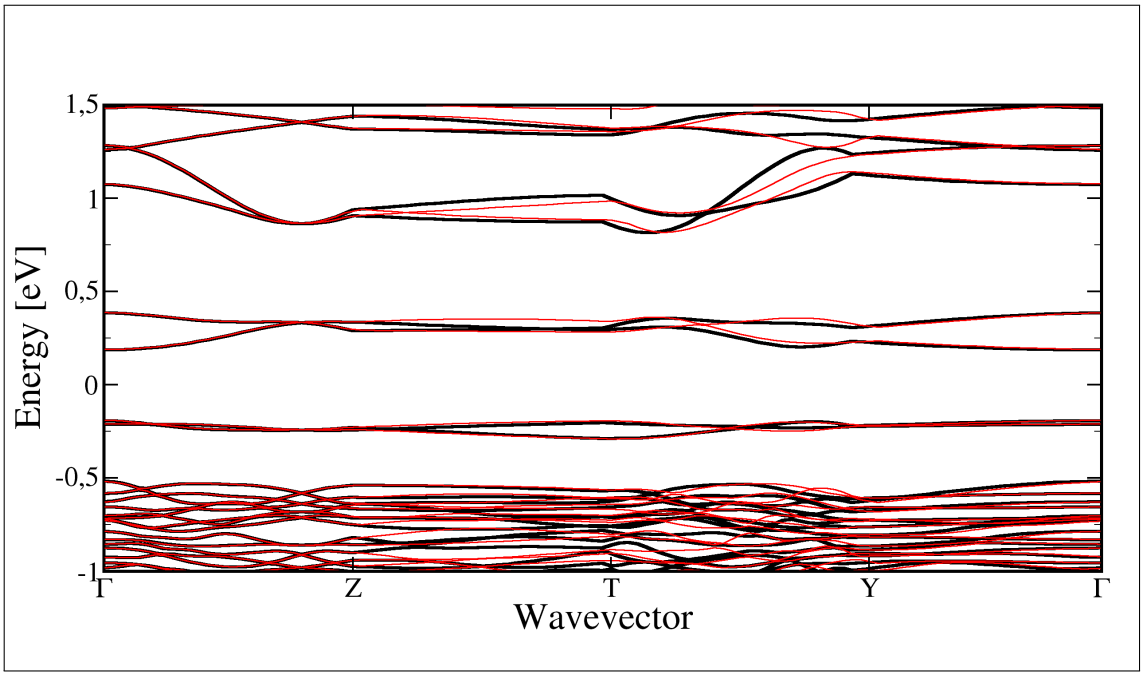

Figure 13 – *Bandstructure of O-O slab. Direct bandgap at the* Γ *point. The Fermi energy is set to zero.*

the previous case, although with opposite spin. Spin down conductive bands have small DOS evenly spread on both elements, which suggests that the excitation would mostly happen towards inner layers. Spin up channel is significantly different, with frontier valence bands being evenly spread over multiple layers with low localization on the surface. The bandstructure in figure 15 shows that the spin up bandgap of 0.22 eV is, in fact, indirect and the direct bandgap has the energy of 0.33 eV.

Changes in charge distribution due to the presence of free surface were evaluated using Bader charge analysis. The inner layers of both slabs agree with the values obtained from bulk hematite. The surface oxygen layer in O-O slab is stabilized by higher charge transfer from iron to oxygen, 0.34 e per Fe-O bond compared to bulk 0.30 e. On the contrary, the bonds between frontier Fe atoms and second O layer show transfer of only 0.28 e per Fe-O bond. In the case of Fe-Fe slab, the charge transfer between surface Fe atoms and first O layer is 0.31 e per Fe-O bond which is close to the bulk value. Other changes at the surface layers are in magnetic moments. The first iron layer is the most affected, as one would expect. While iron atoms have magnetic moments of 4.15 μ_B in bulk hematite, the surface layers change rapidly. For O-O slab, the first Fe layer shows values of 2.80 and 3.66 μ_B for atoms closer

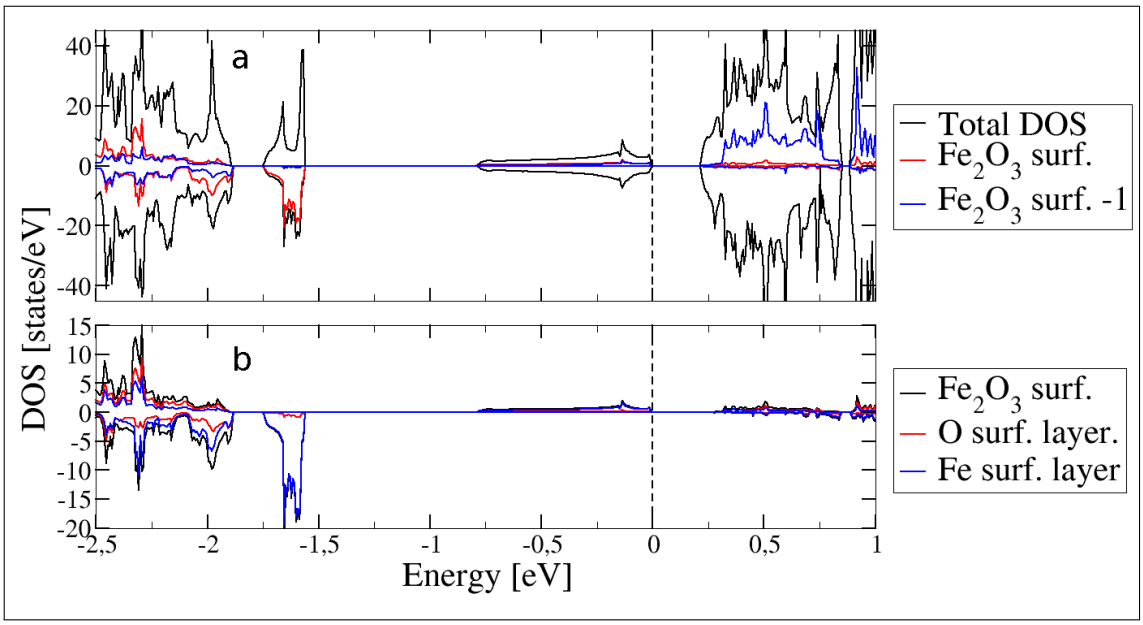

Figure 14 – *(a) total DOS (black) and LDOS for Fe-Fe slab. LDOS for frontier Fe_2O_3 monolayer (red) and for second outer-most monolayer (blue). (b) LDOS contributions from O (red) and Fe (blue) in the first Fe_2O_3 monolayer. Fermi energy is set to zero, marked by the vertical dashed line.*

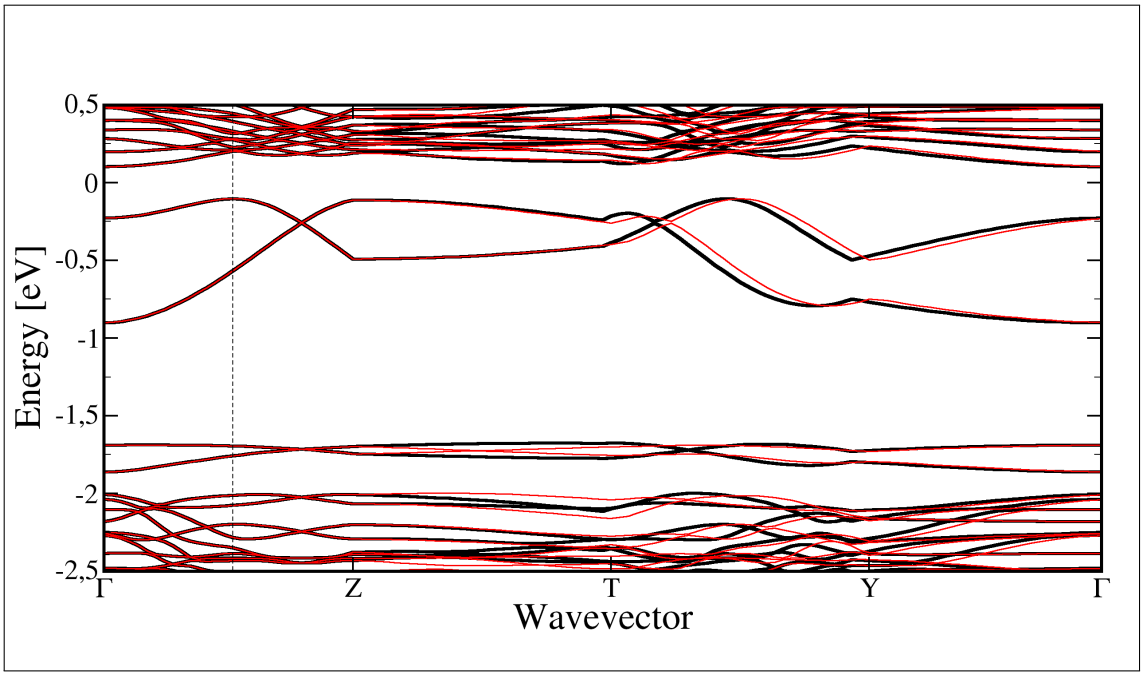

Figure 15 – *Bandstructure of Fe-Fe slab. Indirect bandgap between conductive band minimum (Γ point), valence band maximum (between Γ and Z points. Direct bandgap marked by the vertical dashed line. The Fermi energy is set to zero.*

to surface and bulk, respectively. The second Fe layer has already the value of 4.16 μ_B. The O atoms also have small magnetic moments at the surface. The first two

O layers have 0.22 and 0.12 μ_B per O atom, respectively. Further layers have no magnetic moment. In the Fe-Fe slab, the first Fe layer shows values of 3.84 and 3.63 μ_B for atoms closer to surface and bulk, respectively. The second layer has values of 4.08 and 4.11 μ_B. One can see that the iron atoms, that are closer to the first O layer have somewhat smaller magnetic moments. This is due to the fact that these atoms are closer together than in bulk structure and their magnetic moments interact with each other. The first O layer has a negligible magnetic moment of 0.05 μ_B per atom. Further characterisation of the surface was provided by workfunction calculations.

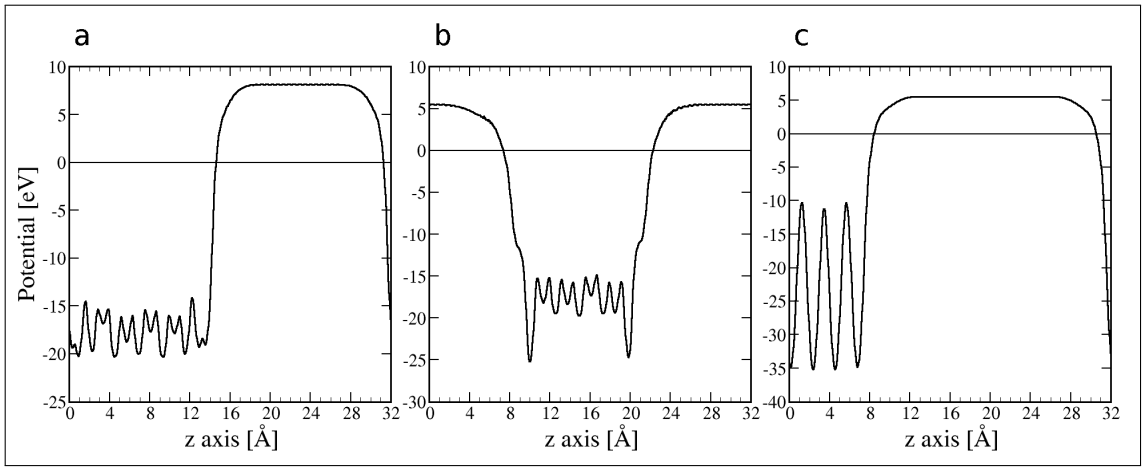

Figure 16 – *The plane average potential of hematite O and Fe terminated slabs, (a) and (b); (c) plane average potential of Pt slab. Potential is plotted against the z vector. The Fermi energy is set to zero.*

Workfunction is defined as the energy needed for an electron to be removed from a surface of a material and therefore is a characteristic property of the surface. It is obtained as the difference of electron potential in a vacuum out of the surface and Fermi level. Plots of plane average potential for all slabs including Pt are shown in figures 16 a-c. The workfunctions obtained from the calculations are 8.1, 5.5 and 5.5 eV for O-O, Fe-Fe and Pt slabs, respectively. These results show a high energetic window for light absorption when excited electrons can potentially contribute to PEC processes before being removed from the material.

4.3. Heterostructures

Slabs of hematite, which were thoroughly discussed above, were placed on top of the Pt slab in order to create a heterostructure with α-Fe_2O_3/Pt interface. All atoms

were allowed to relax, and the optimization criteria were raised gradually. In the end, forces acting on atoms were lower than 1 meV/atom. The optimized heterostructures are illustrated in figure 17 together with the positions of the frontier oxide layer with respect to the first Pt layer. Placing of the O-terminated slab on platinum resulted in O-O-Pt heterostructure, while the Fe-termination led to Fe-Fe-Pt heterostructure. These labels are used hereafter. The evaluation of structural changes was done in

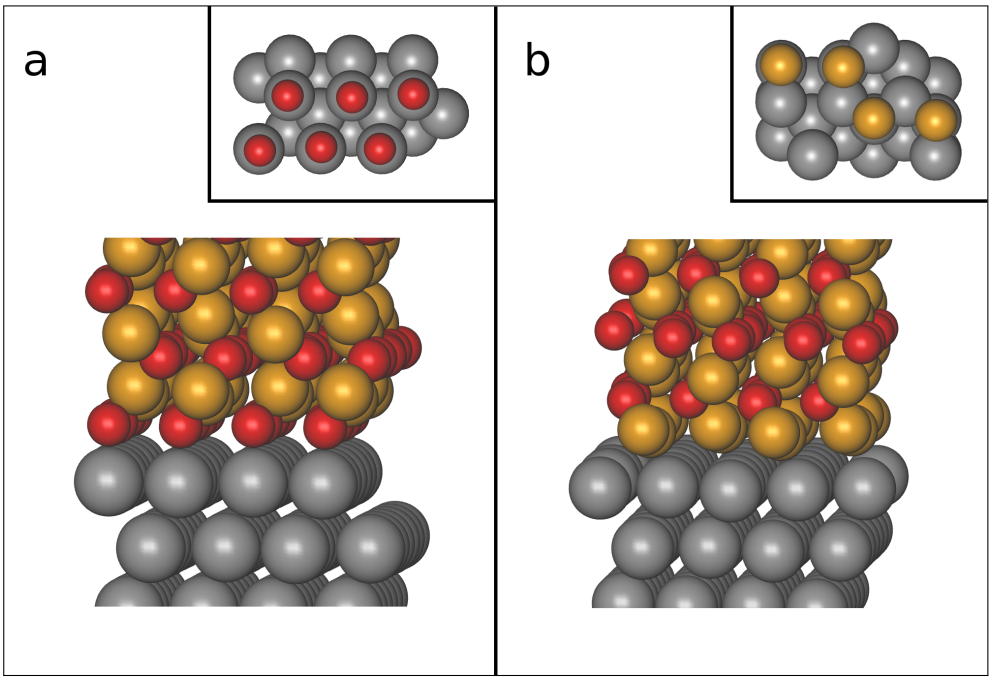

Figure 17 – *Side-view illustration of the interface between (a) O-terminated (b) and Fe-terminated heterostructures. Insets show the arrangement of atoms at the interface.*

the same manner as for slabs. The interface between platinum and oxide exhibits noticeable structural changes compared to bulk oxide. Smaller changes are observed in O-O-Pt heterojunction, which suggests higher interface stability. Table 3 gives summarized values of measured structural changes together with their MAPE. In both heterostructures, the changes are in a range of several percents, with the lowest and highest values being 0.48 and 6.72 %. These intermediate errors suggest that (111) Pt is a suitable support layer for (0001) α-Fe_2O_3. This stability statement is also supported by the bond lengths and respective positions between the frontier layers of oxide and platinum. The O-Pt interface shows that O atoms are stable atop of Pt atoms with O-Pt bond length of 1.961 Å. This bond length is very similar to the Fe-O bond in bulk hematite (1.962 Å). Iron atoms at the Fe-Pt interface stabilize

themselves between three platinum atoms with Fe-Pt bond length of 2.703 Å. This value is lower than Fe-Fe distance in bulk and slabs which can be explained by strong stabilization of unsaturated Fe atoms by platinum layer. Compared with changes in free surfaces, the geometry at the heterojunction is closer to bulk hematite. However, the structural changes are large enough to produce changes in electronic properties, as shown below. The lattice mismatch was minimized in this heterostructure, thus greater structural changes can be expected in real systems.

Table 3 – *Atom distances, bond lengths and angles at the surface layer of both heterostructures showing the interface reconstruction. Distances are given in Angströms. Values in brackets are MAPE in % always compared with bulk values.*

Structure	Fe-O	Fe-Fe	O-O	O..O	∠O-Fe-O
Bulk	1.962	2.996	2.693	2.312	102.53 °
O-O-Pt	1.927 (1.81 %)	2.892 (3.60 %)	2.876 (6.37 %)	2.323 (0.48 %)	96.54 ° (6.20 %)
Fe-Fe-Pt	2.038 (3.72 %)	2.892 (3.59 %)	2.646 (1.78 %)	2.397 (3.55 %)	96.07 ° (6.72 %)

Results from electronic structure calculations show interesting properties induced by the semiconductor/metal junction. Total DOS shows a continuum of states through the Fermi level for both heterostructures, which was expected as originating from the platinum layer. In order to look into the electronic structure of the oxide layer near the interface, the layer-projected DOS was created. It shows a continuum of states in three monolayers closest to the junction in the case of O-O-Pt (fig. 18). As the observed conductive layer does not tell its effect on PEC performance, further analysis of band alignment was performed (fig. 19). Band alignment is based on the unification of Fermi level, which then gives relative positions of bandgaps. For this, a reference point common to all the systems of interest is needed. For slabs, a convenient reference point is the energy of an electron in a vacuum. This is nothing else than workfunction of a given surface. Band alignment graphs are convenient for illustration of charge carrier transport. Holes migrate towards higher energies while electrons migrate towards lower energies. Therefore, type II alignment is required for better charge separation in heterostructures. Figure 19 illustrates the charge carrier transport in macroscopic O-O-Pt material. It consists of four parts : *Pt surface* as the metallic back-contact, Fe_2O_3 *distorted bulk* showing bandgap in non-conductive layers further from heterojunction with Pt, Fe_2O_3 *bulk* representing pristine bulk bandgap, far enough from Pt layer, where the structural distortion disappears, and

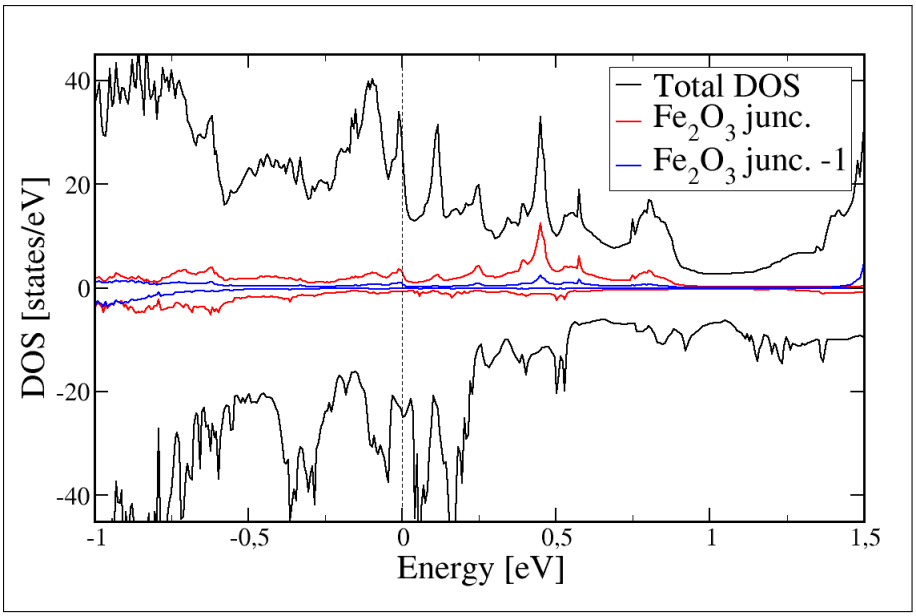

Figure 18 – *O-O-Pt heterostructure. Total DOS (black), LDOS of the first oxide layer from the junction (red), LDOS of the second oxide layer from the junction (blue). Fermi energy is set to zero, marked by the vertical dashed line.*

finally, *O surface* represents trap states at the bare O-terminated hematite surface. The electron transport towards these surface states, marked by an asterisk, can be neglected in a system, where the surface is effectively modified to reduce electron traps. It is clearly visible that this structure enhances charge separation resulting in a lower recombination rate. The electron transport towards the Pt layer is also supported by results from Bader charge analysis. At the O-Pt interface each platinum atom donates 0.32 e per Pt-O bond (bulk Fe-O transfer is 0.30 e), resulting in the total charge of +1.89 e per Pt layer and -5.49 e per O layer at the heterojunction. Deeper into the oxide slab, the charges agree with values from bulk structure : -7.20 e and +7.20 e per O and Fe layer, respectively. The positive charge of the platinum layer together with a lower charge in the first oxygen layer can increase the electron transport from hematite due to lower electrostatic repulsion. This effect lowers the electron-hole recombination rate. These findings are in a strong agreement with the ongoing experiment. Results from experimental measurements showed higher charge separation originating from structure distortions due to the interface with platinum. Better charge separation is caused by charge carriers of opposite signs migrating in opposite directions. Lower hole transfer resistance was also measured by the experiment. Results presented here describe (111) Pt layer as a great substrate for

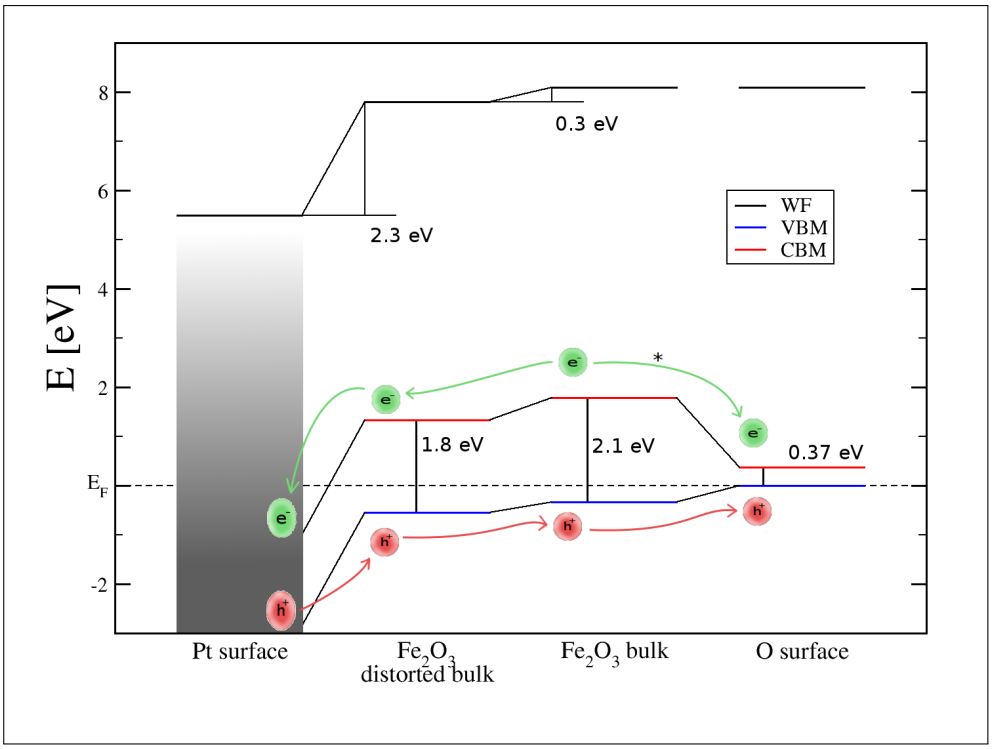

Figure 19 – *Illustration of band bending in the metal-semiconductor junction in O-O-Pt heterostructure. WF, VBM and CBM denote workfunction, valence band maxima and conductive band minima, respectively. The relative positions of bandgaps and WFs are compared with Fermi level which is set to zero, marked by the horizontal dashed line. O surface represents surface states in O-O slab ; Fe_2O_3 bulk represents bulk-like bandgap, taken from the middle layer of O-O slab ; Fe_2O_3 distorted bulk represents bandgap taken from the middle of hematite layer in O-O-Pt heterostructure ; Pt surface represents the metal surface of freestanding Pt slab. Green and red balls and arrows illustrate the migration of electrons and holes, respectively.*
** migration of electrons towards surface states can be excluded via surface modification.*

(0001) hematite for its moderate structural distortions and electronic hybridization, enhancing the PEC performance.

The second heterostructure also shows a continuum of states around the Fermi level for the first oxide monolayer (fig. 20). These states are more visible in the spin down channel while the states in spin up are almost absent. The number of states is lower than in the previous case and disappears immediately after the first layer. Although the interface shows a conductive layer, the electron transport is actually directed from platinum into hematite. This is shown in figure 21. It is clear that the electron transport throughout the oxide layer does not show significant improvement as the conductive band lies around the same energy level. The hole transport is directed towards the Pt layer, which is an undesirable outcome. This

scenario is also supported by the data from Bader charge analysis, which shows, that the first Pt layer has a total charge of -1.79 e and the first Fe layer charge of +5.29 e. This charge difference repels electrons from the heterojunction. Overall results on the Fe-Fe-Pt heterostructure suggest that this system is highly ineffective for PEC water splitting. Changes in magnetic moments were also observed besides

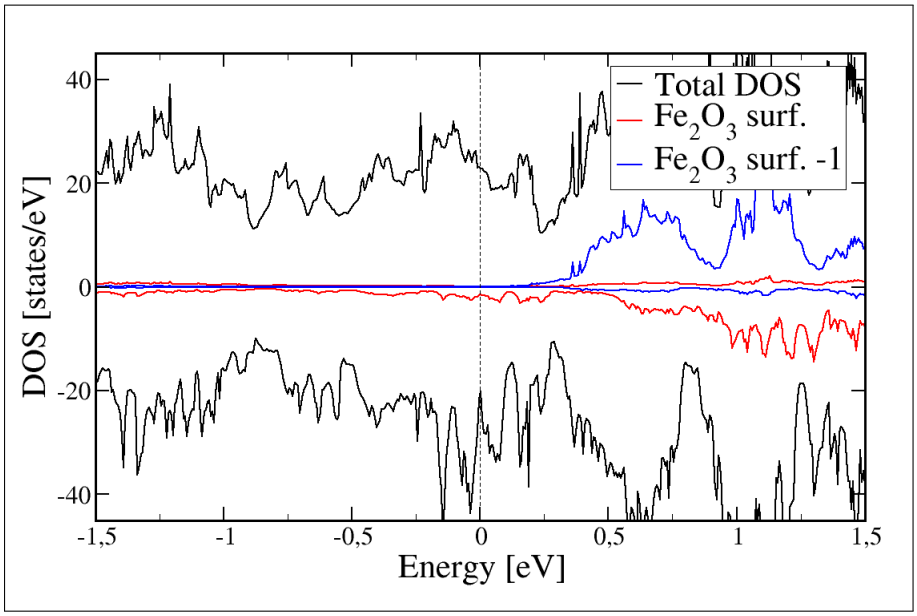

Figure 20 – *Fe-Fe-Pt heterostructure. Total DOS (black), LDOS of the first oxide layer from the junction (red), LDOS of the second oxide layer from the junction (blue). Fermi energy is set to zero, marked by the vertical dashed line.*

DOS and charge analysis. In the case of O-O-Pt interface, magnetic moments are close to 4.15 μ_B. First Fe layer has a magnetic moment of 4.04 μ_B, first O layer 0.05 μ_B and first Pt layer 0.13 μ_B with the opposite moment compared to Fe layer. These results describe (111) Pt layer as a great substrate for (0001) hematite which stabilizes the heterojunction. The hybridization of interface works synergically with geometrical changes and yields great improvement in charge separation.

Iron terminated heterostructure (Fe-Fe-Pt) also shows changes in a magnetic moment, which are closer to bulk-like values, although still very distant compared to O-O-Pt interface. The magnetic moment for the first Fe layer is 3.86 μ_B and the first Pt layer has a magnetic moment of 0.24 μ_B with the same orientation as the Fe layer. This shows the stabilization by Pt layer which adopts the same magnetic ordering as the frontier Fe layer, resulting in the stabilized interface. It shows that platinum can adapt in order to maximally stabilize its counterpart.

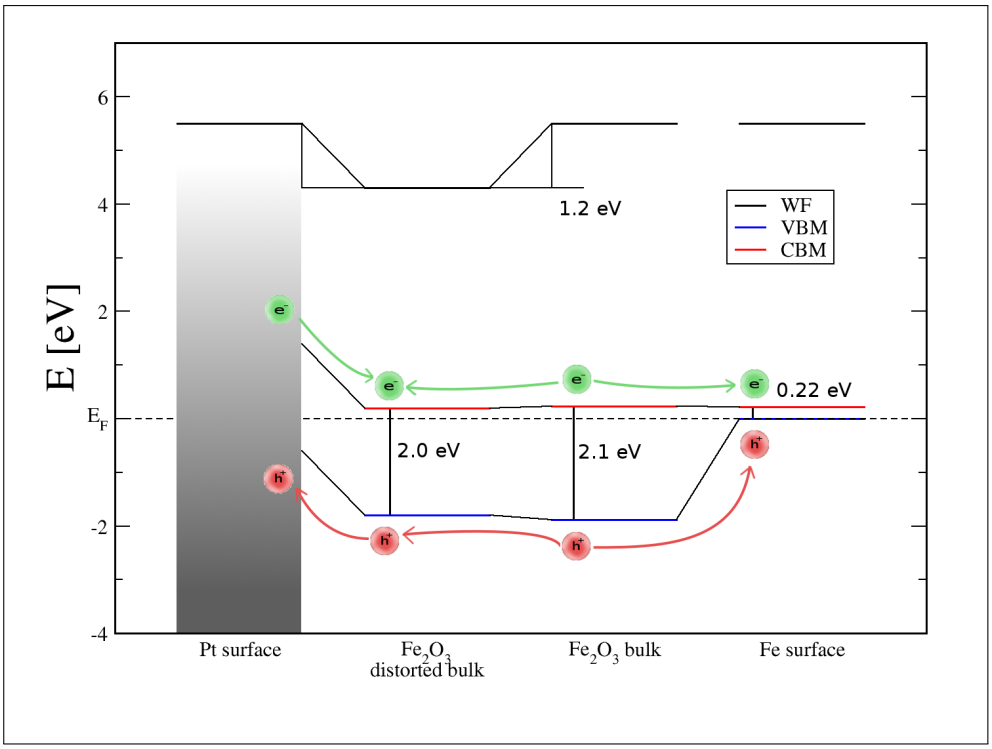

Figure 21 – *Illustration of band bending in the metal-semiconductor junction in Fe-Fe-Pt heterostructure. WF, VBM and CBM denote workfunction, valence band maxima and conductive band minima, respectively. The relative positions of bandgaps and WFs are compared with Fermi level which is set to zero, marked by the horizontal dashed line. Fe surface represents surface states in Fe-Fe slab; Fe_2O_3 bulk represents bulk-like bandgap, taken from the middle layer of Fe-Fe slab; Fe_2O_3 distorted bulk represents bandgap taken from the middle of hematite layer in Fe-Fe-Pt heterostructure; Pt surface represents the metal surface of freestanding Pt slab. Green and red balls and arrows illustrate the migration of electrons and holes, respectively.*

As the last descriptive tool, workfunctions were calculated and compared with the values of freestanding slabs. Plane average potentials of both heterostructures varying with z vector are shown in figure 22. Their respective workfunctions are 7.8 and 4.3 eV. These workfunctions were measured from the oxide surface. It is clear that the heterostructure with a platinum layer somewhat reduces the workfunction of the oxide surface from 8.1 and 5.5 to 7.8 and 4.3 eV, respectively. For the O-terminated surface, the energy needed for photoelectron emission is higher than the energy of ambient incident light. The workfunction of Fe-terminated heterostructure, on the other hand, lies within the spectra of UV-B light, which is present under ambient conditions. The consequence would be that some electrons from the material would be emitted and thus could not participate in PEC processes.

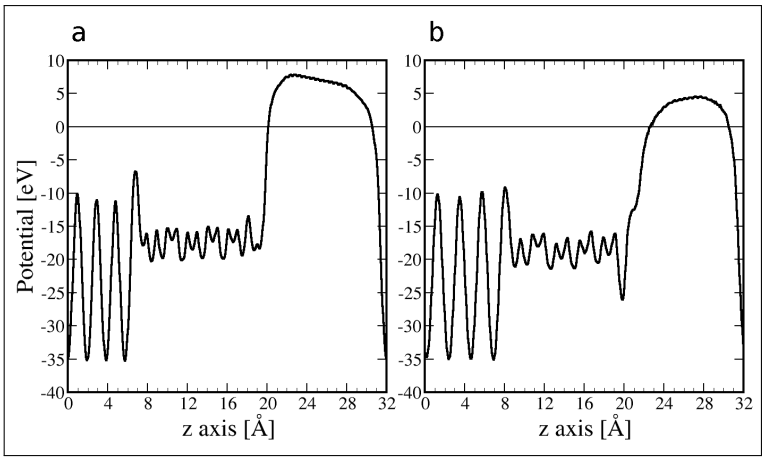

Figure 22 – *The plane average potential of (a) O-O-Pt and (b) Fe-Fe-Pt heterostructures against the z vector. The Fermi energy is set to zero.*

4.4. Pt-doped Hematite

Doping was represented by one Pt atom substituting Fe atom close to surface in relaxed O-O slab (figure 23) in order to analyse its effect on the electronic structure. Relaxation of the structure was done the same way as for a free surface in previous

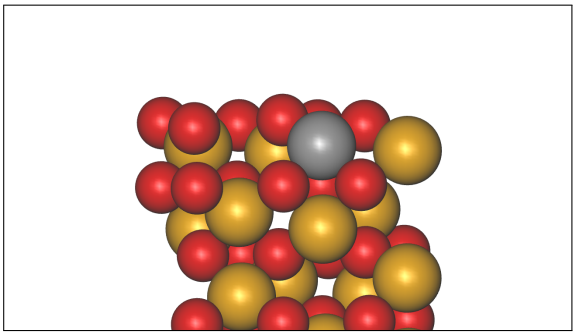

Figure 23 – *Structure of Pt-doped O-O slab.*

chapters. The introduction of a Pt atom into the surface layer resulted in the appearance of new states around Fermi level as shown in figure 24. The graph consists of two LDOS plots, illustrating states that come from the doping atom. The filled cyan curve represents the free surface of the O-terminated oxide slab, summed over a half of the unit cell, opposite to the doped surface. The red curve represents half of the unit cell containing a platinum atom. First glance at the electronic structure can be confusing. One hint for orienting is the fact that the cyan and the red curves would be symmetrical in a case of undoped slab since they represent two opposite halves of the slab. There are significant differences in spin up and spin down chan-

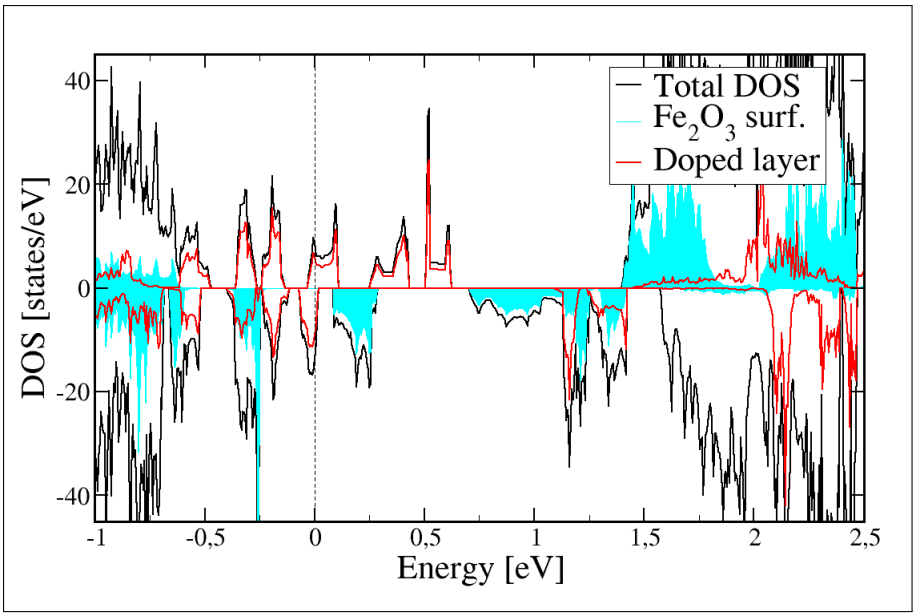

Figure 24 – *Total DOS of a single-doped slab (black); filled curve illustrates the contribution of pristine O-terminated surface (cyan); states originating in Pt-doped surface layer (red). Fermi energy is set to zero, marked by the dashed line.*

nels, starting from -0.6 eV. There are states in both channels around the Fermi level which results in no bandgap. One can see that the states are strongly localized at the surface layer, barely reaching to other layers (small difference between black and red curves). These localized states around the Fermi level would trap charge carriers and allow their prompt recombination. Data obtained from Bader charge analysis show that the Pt atom acts as an electron donor to surrounding O atoms. The difference is in the magnetic moment distribution, where the iron layer keeps values similar to those in free surface but platinum has a magnetic moment of 0.66 μ_B with an opposite sign than the iron layer. Also, three closest O atoms to the doping atom have opposite magnetic moments than the iron layer. These changes in magnetic moments inside a monolayer disrupt the magnetic ordering of the material and can explain the differences between both spins in LDOS of the doped layer. Instead of showing states in only one spin channel due to the magnetic moment of that layer, midgap states are observed in both channels, however, not completely symmetrical. The overview of the changes with the introduction of Pt dopant shows that platinum is not beneficial for surface modification towards better PEC performance. The doping introduces surface localized states that would effectively reduce charge separation leading towards low performance.

5. Summary

The pursuit of so-called green energy is going through an intense phase, where we have several known processes that we can use, but their efficiency is still a problem. Experimental groups developing various devices for the harvesting of solar energy and its conversion are often accompanied by theoreticians who help to understand the processes inside these innovative materials. This thesis is aimed to describe the properties of an interface between (0001) α-hematite and (111) platinum using DFT+U methods. This heterosystem was prepared by the experimental group in the Regional centre of advanced technologies and materials (RCPTM) and exhibited superior photovoltaic properties against commonly used FTO substrate.

We modelled two different surfaces of the hematite layer in order to describe the differences in electronic structure coming from the surface termination. These structures consist of oxygen and iron terminated surfaces. Their structural changes were compared with bulk values to show the magnitude of changes. The changes were pronounced in the range of few percents, with exception of the positions of the surface-most iron atoms. The changes in Fe-O bond lengths and O-Fe-O angles reach up to 12 %. The electronic structure analysis showed that hematite free surfaces are not suitable for PEC water splitting due to narrow bandgaps, less than 0.5 eV, originating in surface states. Another drawback in the application of bare hematite surface as photoanode material is the different electronic structure for each spin channel.

Hematite slabs were placed on top of the platinum layer to form heterostructure as prepared in the experiments. Both structures exhibited structural changes that partially restored bulk-like geometry near the interface. This was the first hint that platinum can be a suitable substrate for the hematite layer. Analysis of the electronic structure showed conductivity in a few layers at the interface which can contribute to better performance in PEC water splitting by draining the excited electrons from hematite to platinum substrate. The observed conductive interface was more pronounced in the oxygen-terminated junction. The main reason for strong hybridization between platinum and oxygen atoms is the arrangement at the interface, where each O atom binds with one Pt. Minimal lattice mismatch allowed relaxation of the surface towards bulk-like structure and hybridization with more

layers of oxide, creating a deeper conductive layer. Both heterostructures were also studied in the matter of charge separation, which showed superior properties of O-O-Pt heterostructure over Fe-Fe-Pt. The results showed beneficial band alignment throughout the structure. This increases the charge separation and guides holes onto the oxide surface and electrons towards platinum. Holes concentrated on the oxide surface can react with water molecules and electrons are lead to the cathode where they participate in HER. This study also gives a hint on how to modify the oxide surface towards better PEC performance. That is to keep the valence band maximum close to Fermi level, wide bandgap and of course good catalytic properties. The latter is a subject for extensive research, whose mechanism is not completely clear.

In the last part, the Pt-doped hematite surface was studied in order to see the influence of doping Pt atom on the electronic structure of hematite. It was found that platinum as a substituent of iron is not suitable for PEC applications for the absence of bandgap and the creation of surface trap states. Localized continuum of states around the Fermi level is the centre of electron-hole recombination.

This thesis gives a theoretical insight into the (0001) α-Fe_2O_3/(111) Pt interface, explaining its benefits for the application in PEC water splitting cells. The study of hematite surface shows some drawbacks of bare hematite surface. There are several possible future developments in the study of this heterostructure, e.g. calculations of electric conductivity through the interface, OER mechanism, surface modification. Although the theoretical study of hematite is fairly complicated using DFT methods, approximations and combinations of methods are available for these purposes. Nonetheless, new methods have to be developed in this field of material chemistry to better describe and understand the crucial properties in this highly anticipated field.

6. Závěr

Snaha o tzv. zelenou energii prochází intenzivní fází, kdy známe několik známých procesů, které můžeme využít, ale jejich účinnost je stále problém. Experimentální skupiny, které vyvíjejí různá zařízení pro sběr sluneční energie a její přeměnu, jsou často doprovázeny teoretiky, kteří pomáhají pochopit procesy uvnitř těchto inovativních materiálů. Cílem této práce je popsat vlastnosti rozhraní mezi (0001) α-hematitem a (111) platinou metodami DFT+U. Tento heterosystém byl připraven experimentální skupinou v Regionálním centru pokročilých technologií a materiálů (RCPTM) a vykazoval vynikající fotovoltaické vlastnosti proti běžně používanému substrátu FTO.

Připravili jsme dva různé povrchy vrstvy hematitu, abychom popsali rozdíly v elektronové struktuře, která vychází ze struktury povrchu. Tyto struktury se skládají z kyslíkem a železem ukončených povrchů. Jejich strukturální změny byly porovnány s hodnotami pro bulk, aby ukázaly jejich velikost. Změny byly zřetelné v rozsahu několika procent, s výjimkou poloh atomů železa nejblíže povrchu. Změny v délkách vazeb Fe-O a O-Fe-O dosahují až 12 %. Elektronická analýza struktury ukázala, že volné povrchy hematitu nejsou vhodné pro štěpení vody PEC v důsledku úzkých zakázaných pásů, menších než 0,5 eV, pocházejících z povrchových stavů. Další nevýhodou při použití čistého povrchu hematitu jako materiálu pro fotoanodu je odlišná elektronická struktura pro každý spin.

Vrstvy hematitu byly umístěny na vrstvu platiny, čímž byla vytvořena heterostruktura, popsána v experimentech. Obě struktury vykazovaly strukturální změny, které částečně obnovily symetrickou geometrii poblíž rozhraní. To byl první náznak, že platina může být vhodným substrátem pro hematit. Analýza elektronové struktury ukázala vodivost v několika vrstvách na rozhraní, která může přispět k lepšímu výkonu při štěpení vody PEC odváděním excitovaných elektronů z hematitu do platinového substrátu. Pozorované vodivé rozhraní bylo výraznější na spoji zakončeném kyslíkem. Hlavním důvodem silné hybridizace mezi atomy platiny a kyslíku je uspořádání na rozhraní, kde se každý atom O váže s jedním tomem Pt. Minimální rozdíl krystalových mřížek umožnil relaxaci povrchu směrem k bulkové struktuře a hybridizaci s více vrstvami oxidu, čímž se vytvořila hlubší vodivá vrstva. Obě heterostruktury byly studovány také z hlediska separace nábojů, která ukázala lepší vlastnosti O-

O-Pt heterostruktury oproti Fe-Fe-Pt. Výsledky ukázaly příznivé uspořádání pásů v celé struktuře. To zvyšuje separaci nábojů. Navíc vede díry na povrch oxidu a elektrony směrem k platině. Díry koncentrované na povrchu oxidu mohou reagovat s molekulami vody a elektrony jsou odvedeny na katodu, kde se účastní HER. Tato studie také naznačuje, jak modifikovat povrch hematite směrem k lepšímu výkonu v PEC rozkladu vody. Tedy udržet maximum valenčního pásu blízko Fermiho hladiny, široký zakázaný pás a samozřejmě dobré katalytické vlastnosti povrchu. Poslední zíněný jev je předmětem rozsáhlého výzkumu, jehož mechanismus není zatím zcela jasný.

V poslední části byl studován povrch hematitu dopovaný Pt, abychom zjistili vliv dopujícího atomu Pt na elektronovou strukturu hematitu. Bylo zjištěno, že platina jako substituent železa není vhodná pro aplikace PEC pro nepřítomnost zakázaného pásu a vytváření povrchových pastí. Lokalizované kontinuum stavů kolem Fermiho hladiny je centrem rekombinace elektronů a děr.

Tato práce poskytuje teoretický pohled na rozhraní (0001) α-Fe_2O_3/(111) Pt, vysvětlující jeho přínosy pro aplikaci v zařízeních pro PEC štěpení vody. Studium povrchu hematitu ukazuje některé nevýhody čistého povrchu. Pro studium tohoto systému existuje několik možných budoucích směrů, např. výpočty elektrické vodivosti skrze rozhraní, mechanismus OER nebo modifikace povrchu. I když je teoretické studium hematitu metodami DFT poměrně komplikované, pro tyto účely jsou k dispozici aproximace a kombinace metod. V této oblasti výpočetní chemie však musí být vyvinuty nové metody, které by lépe popsaly a pochopily klíčové vlastnosti tohoto vysoce perspektivního oboru.

7. Bibliography

[1] Y. Tachibana, L. Vayssieres, and J. R. Durrant. Artificial photosynthesis for solar water-splitting. *Nature Photonics*, 6(8) :511–518, jul 2012, doi :10.1038/nphoton.2012.175.

[2] D. G. Nocera. Solar Fuels and Solar Chemicals Industry. *Accounts of Chemical Research*, 50(3) :616–619, mar 2017, doi :10.1021/acs.accounts.6b00615.

[3] K. Sivula, F. Le Formal, and M. Grätzel. Solar water splitting : progress using hematite (α-Fe_2O_3) photoelectrodes. *ChemSusChem*, 4(4) :432–49, 2011, doi :10.1002/cssc.201000416.

[4] A. Fujishima and K. Honda. Electrochemical Photolysis of Water at a Semiconductor Electrode. *Nature*, 238(5358) :37–38, jul 1972, doi :10.1038/238037a0.

[5] M. D. Bhatt and J. S. Lee. Recent theoretical progress in the development of photoanode materials for solar water splitting photoelectrochemical cells. *J. Mater. Chem. A*, 3(20) :10632–10659, 2015, doi :10.1039/C5TA00257E.

[6] T. Jafari, E. Moharreri, A. Amin, R. Miao, W. Song, and S. Suib. Photocatalytic Water Splitting-The Untamed Dream : A Review of Recent Advances. *Molecules*, 21(7) :900, 2016, doi :10.3390/molecules21070900.

[7] M. Barroso, S. R. Pendlebury, A. J. Cowan, and J. R. Durrant. Charge carrier trapping, recombination and transfer in hematite (α-Fe_2O_3) water splitting photoanodes. *Chemical Science*, 4(7) :2724, 2013, doi :10.1039/c3sc50496d.

[8] N. Yatom, O. Neufeld, and M. C. Toroker. Toward Settling the Debate on the Role of Fe_2O_3 Surface States for Water Splitting. *Journal of Physical Chemistry C*, 119(44) :24789–24795, 2015, doi :10.1021/acs.jpcc.5b06128.

[9] B. Klahr, S. Gimenez, F. Fabregat-Santiago, T. Hamann, and J. Bisquert. Water Oxidation at Hematite Photoelectrodes : The Role of Surface States. *Journal of the American Chemical Society*, 134(9) :4294–4302, mar 2012, doi :10.1021/ja210755h.

[10] L. Xi, S. Y. Chiam, W. F. Mak, P. D. Tran, J. Barber, S. C. J. Loo, and L. H. Wong. A novel strategy for surface treatment on hematite photoanode for efficient water oxidation. *Chem. Sci.*, 4(1) :164–169, 2013, doi :10.1039/C2SC20881D.

[11] A. G. Tamirat, J. Rick, A. A. Dubale, W. Su, and B. Hwang. Using hematite for photoelectrochemical water splitting : a review of current progress and challenges. *Nanoscale Horiz.*, 1(4) :243–267, 2016, doi :10.1039/C5NH00098J.

[12] Š. Kment, Z. Hubička, M. Allieta, J. Tuček, Y. Rambabu, G. Zoppellaro, A. Matěj, P. Blonski, H. Kmentová, A. Naldoni, M. Otypeka, P. Schmuki and R. Zbořil. *Unpublished manuscript*, 2019.

[13] W. Koch and M. C. Holthausen. *A Chemist ' s Guide to Density Functional Theory*, volume 3. Wiley-VCH Verlag GmbH, 2001.

[14] D. S. Sholl and J. A. Steckel. *Density Functional Theory : A Practical Introduction*. John Wiley & Sons, Inc., 2009.

[15] P. Hohenberg and W. Kohn. Inhomogeneous Electron Gas. *Physical Review*, 136(3B) :B864–B871, nov 1964, doi :10.1103/PhysRev.136.B864.

[16] W. Kohn and L. J. Sham. Self-Consistent Equations Including Exchange and Correlation Effects. *Physical Review*, 140(4A) :A1133–A1138, nov 1965, doi :10.1103/PhysRev.140.A1133.

[17] R. G. Parr and Y. Weitao. *Density-Functional Theory of Atoms and Molecules*. International Series of Monographs on Chemistry. Oxford University Press, 1994.

[18] J. P. Perdew and Y. Wang. Accurate and simple analytic representation of the electron-gas correlation energy. *Physical Review B*, 45(23) :13244–13249, jun 1992, doi :10.1103/PhysRevB.45.13244.

[19] J. P. Perdew, K. Burke, and M. Ernzerhof. Generalized Gradient Approximation Made Simple. *Physical Review Letters*, 77(18) :3865–3868, 1996, doi :10.1103/PhysRevLett.77.3865.

[20] J. P. Perdew, S. Kurth, A. Zupan, and P. Blaha. Accurate density functional with correct formal properties : A step beyond the generalized gradient approximation. *Physical Review Letters*, 82(12) :2544–2547, 1999, doi :10.1103/PhysRevLett.82.2544.

[21] A. D. Becke. A new mixing of Hartree-Fock and local density-functional theories. *The Journal of Chemical Physics*, 98(2) :1372–1377, 1993, doi :10.1063/1.464304.

[22] J. H. de Boer and E. J. W. Verwey. Semi-conductors with partially and with completely filled 3d-lattice bands. *Proceedings of the Physical Society*, 49(4S) :59–71, aug 1937, doi :10.1088/0959-5309/49/4S/307.

[23] N. F. Mott and R. Peierls. Discussion of the paper by de Boer and Verwey. *Proceedings of the Physical Society*, 49(4S) :72–73, aug 1937, doi :10.1088/0959-5309/49/4S/308.

[24] N. F. Mott. The Basis of the Electron Theory of Metals, with Special Reference to the Transition Metals. *Proceedings of the Physical Society. Section A*, 62(7) :416–422, jul 1949, doi :10.1088/0370-1298/62/7/303.

[25] J. Hubbard. Electron Correlations in Narrow Energy Bands. *Proceedings of the Royal Society A : Mathematical, Physical and Engineering Sciences*, 276(1365) :238–257, nov 1963, doi :10.1098/rspa.1963.0204.

[26] W. J. Hehre, K. Ditchfield, and J. A. Pople. Self-consistent molecular orbital methods. XII. Further extensions of gaussian-type basis sets for use in molecular orbital studies of organic molecules. *The Journal of Chemical Physics*, 56(5) :2257–2261, 1972, doi :10.1063/1.1677527.

[27] T. H. Dunning. Gaussian basis sets for use in correlated molecular calculations. I. The atoms boron through neon and hydrogen. *The Journal of Chemical Physics*, 90(2) :1007–1023, 1989, doi :10.1063/1.456153.

[28] P. C. Hariharan and J. A. Pople. The influence of polarization functions on molecular orbital hydrogenation energies. *Theoretica Chimica Acta*, 28(3) :213–222, 1973, doi :10.1007/BF00533485.

[29] G. Kresse and J. Furthmuller. Efficiency of ab-initio total energy calculations for metals and semiconductors using a plane-wave basis set. *Computational Materials Science*, 6(1) :15–50, jul 1996, doi :10.1016/0927-0256(96)00008-0.

[30] F. Bloch. Über die Quantenmechanikder Elektronen in Kristallgittern . *Zeitschrift für Physik A Hadrons and Nuclei*, 52(7) :555–600, 1928, doi :http ://dx.doi.org/10.1007/BF01339455.

[31] H. Hellmann. A New Approximation Method in the Problem of Many Electrons. *The Journal of Chemical Physics*, 3(1) :61–61, jan 1935, doi :10.1063/1.1749559.

[32] W. Quester. Sketch Pseudopotentials. URL :https ://commons.wikimedia.org/wiki-/File :Sketch_Pseudopotentials.png, Accessed 17.4.2019.

[33] P. E. Blöchl. Projector augmented-wave method. *Physical Review B*, 50(24) :17953–17979, 1994, doi :10.1103/PhysRevB.50.17953.

[34] J. Hafner. Ab-initio simulations of materials using VASP : Density-functional theory and beyond. *Journal of Computational Chemistry*, 29(13) :2044–2078, oct 2008, doi :10.1002/jcc.21057.

[35] G. Kresse and D. Joubert. From ultrasoft pseudopotentials to the projector augmented-wave method. *Physical Review B*, 59(3) :1758–1775, 1999, doi :10.1103/PhysRevB.59.1758.

[36] C. Kittel. *Introduction to solid state physics*. Wiley, eighth edition, 2005.

[37] N. Large. *Resonant Raman-Brillouin scattering in semiconductor and metallic nanostructures : from nano-acoustics to acousto-plasmonics.* dissertation, Université Toulouse III Paul Sabatier (UT3 Paul Sabatier), and Universidad del País Vasco (UPV/EHU), 2011.

[38] A. I. Liechtenstein, V. I. Anisimov, and J. Zaanen. Density-functional theory and strong interactions : Orbital ordering in Mott-Hubbard insulators. *Physical Review B*, 52(8) :5467–5471, 1995, doi :10.1103/PhysRevB.52.R5467.

[39] S. L. Dudarev, G. A. Botton, S. Y. Savrasov, C. J. Humphreys, and A. P. Sutton. Electron-energy-loss spectra and the structural stability of nickel oxide : An LSDA+U study. *Physical Review B*, 57(3) :1505–1509, jan 1998, doi :10.1103/PhysRevB.57.1505.

[40] N. Dzade, A. Roldan, and N. de Leeuw. A Density Functional Theory Study of the Adsorption of Benzene on Hematite (α-Fe_2O_3) Surfaces. *Minerals*, 4 :89–115, 2014, doi :10.3390/min4010089.

[41] Y. Guo, S. J. Clark, and J. Robertson. Electronic and magnetic properties of Ti_2O_3 , Cr_2O_3 , and Fe_2O_3 calculated by the screened exchange hybrid density functional. *Journal of Physics : Condensed Matter*, 24(32) :325504, 2012, doi :10.1088/0953-8984/24/32/325504.

[42] H. Han, F. Riboni, F. Karlicky, S. Kment, A. Goswami, P. Sudhagar, J. Yoo, L. Wang, O. Tomanec, M. Petr, O. Haderka, C. Terashima, A. Fujishima, P. Schmuki, and R. Zboril. α-Fe_2O_3/TiO_2 3D hierarchical nanostructures for enhanced photoelectrochemical water splitting. *Nanoscale*, 9(1) :134–142, 2017, doi :10.1039/c6nr06908h.

[43] A. Kiejna and T. Pabisiak. Surface properties of clean and Au or Pd covered hematite (α-Fe_2O_3) (0001). *Journal of physics. Condensed matter : an Institute of Physics journal*, 24(9) :095003, 2012, doi :10.1088/0953-8984/24/9/095003.

[44] O. Neufeld and M. C. Toroker. Platinum-Doped α-Fe_2O_3 for Enhanced Water Splitting Efficiency : A DFT+U Study. *The Journal of Physical Chemistry C*, 119(11) :5836–5847, mar 2015, doi :10.1021/jp512002f.

[45] O. Neufeld and M. C. Toroker. Can we judge an oxide by its cover ? The case of platinum over α-Fe_2O_3 from first principles. *Phys. Chem. Chem. Phys.*, 17(37) :24129–24137, 2015, doi :10.1039/C5CP04314J.

[46] P. Merchant, R. Collins, R. Kershaw, K. Dwight, and A. Wold. The Electrical, Optical and Photoconducting Properties of $Fe_{c-x}Cr_xO_3$ ($0 \leq x \leq 0.47$). *Journal of Solid State Chemistry*, 27(3) :307–315, mar 1979, doi :10.1016/0022-4596(79)90173-7.

[47] E. Kren, P. Szabo, and G. Konczos. Neutron diffraction studies on the (1-x) Fe_2O_3 - xRh_$2O_3$ system. *Physics Letters*, 19(2) :103–104, oct 1965, doi :10.1016/0031-9163(65)90731-6.

[48] J. M. D. Coey and G. A. Sawatzky. A study of hyperfine interactions in the system $(Fe_{1-x}Rh_x)_2O_3$ using the Mossbauer effect (Bonding parameters). *Journal of Physics C : Solid State Physics*, 4(15) :2386–2407, oct 1971, doi :10.1088/0022-3719/4/15/025.

[49] G. Rollmann, A. Rohrbach, P. Entel, and J. Hafner. First-principles calculation of the structure and magnetic phases of hematite. *Physical Review B*, 69(16) :165107, 2004, doi :10.1103/PhysRevB.69.165107.

[50] E. N. Maslen, V. A. Streltsov, N. R. Streltsova, and N. Ishizawa. Synchrotron X-ray study of the electron density in α-Fe_2O_3. *Acta Crystallographica Section B Structural Science*, 50(4) :435–441, aug 1994, doi :10.1107/S0108768194002284.

[51] F. Birch. Finite Elastic Strain of Cubic Crystals. *Physical Review*, 71(11) :809–824, jun 1947, doi :10.1103/PhysRev.71.809.

[52] G. Glockler. The Structure of Crystals. By Ralph W. G. Wyckoff. *The Journal of Physical Chemistry*, 40(3) :422–422, jan 1935, doi :10.1021/j150372a016.

[53] G. Henkelman, A. Arnaldsson, and H. Jonsson. A fast and robust algorithm for Bader decomposition of charge density. *Computational Materials Science*, 36(3) :354–360, jun 2006, doi :10.1016/j.commatsci.2005.04.010.

[54] E. Sanville, S. D. Kenny, R. Smith, and G. Henkelman. Improved grid-based algorithm for Bader charge allocation. *Journal of Computational Chemistry*, 28(5) :899–908, apr 2007, doi :10.1002/jcc.20575.

[55] W. Tang, E. Sanville, and G. Henkelman. A grid-based Bader analysis algorithm without lattice bias. *Journal of Physics : Condensed Matter*, 21(8) :084204, feb 2009, doi :10.1088/0953-8984/21/8/084204.

[56] A. Kiejna and T. Pabisiak. Mixed Termination of Hematite (α-Fe_2O_3)(0001) Surface. *The Journal of Physical Chemistry C*, 117(46) :24339–24344, nov 2013, doi :10.1021/jp406946s.

[57] R. Lebrun, A. Ross, S. A. Bender, A. Qaiumzadeh, L. Baldrati, J. Cramer, A. Brataas, R. A. Duine, and M. Kläui. Tunable long-distance spin transport in a crystalline antiferromagnetic iron oxide. *Nature*, 561(7722) :222–225, 2018, doi :10.1038/s41586-018-0490-7.